Experimental and theoretical evaluation of the anticorrosive proprieties of new 1,2,3-triazolyl-acridine derivatives

Caio Machado Fernandes [a], Renato C.S. Lessa [b], Dora C.S. Costa [c], Lucas Guedes [a],
Vinicius Martins [a], Awad A. Al-Rashdi [d], Vitor Francisco Ferreira [c], Fernando de C. da Silva [c],
Júlio César M. Silva [a], Marcela C. de Moraes [b], Hassane Lgaz [e,**], Eduardo A. Ponzio [a,*]

[a] *Laboratório de Materiais da UFF, Instituto de Química, Universidade Federal Fluminense, Niterói, 24020-141, Rio de Janeiro, Brazil*
[b] *BioCrom, Laboratório de Cromatografia de Bioafinidade e Química Ambiental, Instituto de Química, Universidade Federal Fluminense, Niterói, 24020-141, Rio de Janeiro, Brazil*
[c] *LabSOA, Laboratório de Síntese Orgânica Aplicada, Instituto de Química, Universidade Federal Fluminense, Niterói, 24020-141, Rio de Janeiro, Brazil*
[d] *Chemistry Department, Umm Al-Qura University, Al-Qunfudah University College, Saudi Arabia*
[e] *Innovative Durable Building and Infrastructure Research Center, Center for Creative Convergence Education, Hanyang University ERICA, 55 Hanyangdaehak-ro, Sangrok-gu, Ansan-si, Gyeonggi-do 15588, Republic of Korea*

ARTICLE INFO

ABSTRACT

Three novel 1,2,3-triazolyl-acridine derivatives (abbreviated as TTA, ATM, and ATA) were synthesized via a fast ultrasound-assisted copper-catalyzed azide-alkyne cycloaddition (CuAAC) in good yields. They were studied as corrosion inhibitors for 1020 mild steel in acidic media (1 mol/L HCl) using gravimetric and electrochemical measurements. Weight Loss Study showed that those molecules have anticorrosive efficiency varying from 85 to 94 % at 1 mmol/L (298 K). They also increased their corrosion mitigation at higher temperatures, reaching up to 90–96 % at 338 K. Isotherm fitting revealed that all developed corrosion inhibitors follow the Langmuir theory and data crossing confirmed the monolayer formation. Atomic Force Microscopy suggested the presence of a protective film on the metal surface and Electrochemical Impedance Spectroscopy, Linear Polarization Resistance, and Electrochemical Frequency Modulation showed a better charge transfer and polarization resistance alongside a lower corrosion current density in the presence of TTA, ATM, and ATA in the corrosive media. Also, polarization curves characterized all three organic molecules as mixed-type corrosion inhibitors for mild steel. First-principles density functional theory (DFT) simulations revealed that all molecules form covalent bonds with iron atoms upon adsorption on Fe(1 1 0) surface. The ATA molecule exhibited a bond-breaking upon adsorption and had a higher interaction energy with the iron surface. The chemical interactions between inhibitors' molecules and iron atoms were confirmed by projected density of states analysis, showing a strong hybridization between molecules' orbitals and 3d iron orbitals.

1. Introduction

The use of mild steel, a common material in various structures and applications because of its affordable price and good physical properties, is associated with several problems when exposed to acid medium, as in the cleaning and maintenance process, that occur not only at room temperature but at higher ones, showing high vulnerability. Because of this issue, pipes, reactors, and others devices based on this material can present several hazards to human life and the environment. In addition, processes that occur when mild steel is exposed to acidic substances require high costs in repairs and replacements when damaged by corrosion (Rajamohan et al., 2022a, Rajamohan et al., 2022b, Ren et al., 2022).

Aiming to control this problem, the use of organic corrosion inhibitors (OCIs) has been common and widely studied to protect the steel surface from possible chemical attacks caused by the environment to
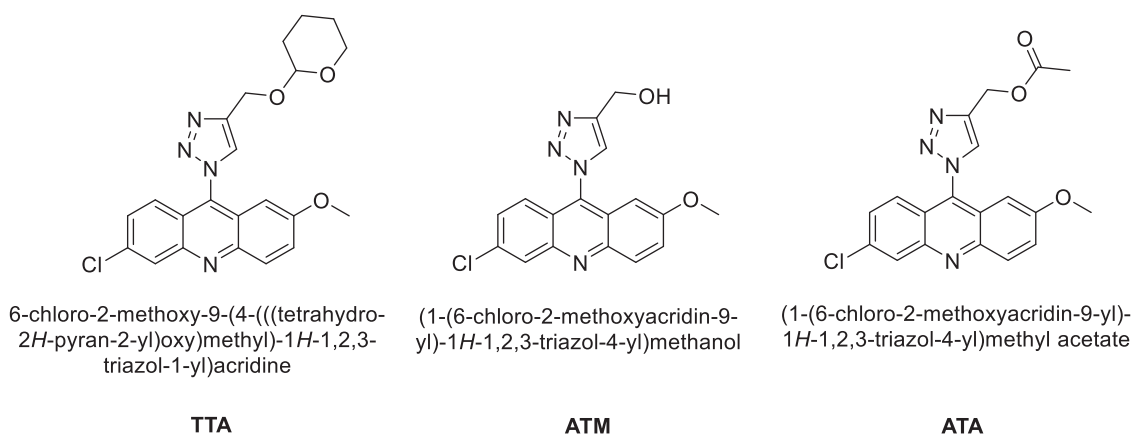
Fig. 1. Molecular structure of the synthesized and evaluated 1,2,3-triazolyl-acridine derivatives.

which it is exposed (Zheng et al., 2022). By adsorbing on the surface of the material, the inhibitor can curb the corrosion process through interaction between the active sites, forming a protective film. The efficiency of the molecule as a corrosion inhibitor is directly related to its adsorption to the material. The more interactions of the substance with the steel, the greater the area covered (Zhang et al., 2022). That can be given by physical adsorption processes, which depend on the structure and electrostatic interaction; and/or by chemical reactions, carried out through the presence of heteroatoms with non-bonding electron pairs and π–electrons interacting with vacant d orbitals (Tan et al., 2022, Wu et al., 2022).

Among the structural characteristics that make a compound a possible corrosion inhibitor, it is highlighted the presence of Lewis basic sites. These are common in inorganic and organic compounds. While the former used to be widely applied due to its high oxidative power, the organic ones have been standing out for being cheap, less toxic, and commonly environmental-friendly when compared to the inorganic ones (highly toxic for human health and nature), maintaining or improving inhibition efficiency (El-Lateef et al., 2022, El Faydy et al., 2022, Molaeipour et al., 2022).

Thus, organic compounds containing a heterocyclic nitrogen chain, such as acridine, a three-ring structure with two benzene rings linked by a nitrogen atom and a —CH═group, have been investigated as corrosion inhibitors (Zhang et al., 2019a, Zhang et al., 2019b, Zhang et al., 2020a, Zhang et al., 2020b, Zhang et al., 2020c, Altunbaş Şahin, 2022). One of the features that make acridine-based compounds the object of interest of several works focused on corrosion inhibitors is the fact that acridine-derivatives contain a polar unit relative to the nitrogen atom. Moreover, their large conjugated system has been described as an advantage for these inhibitors (Akpan et al., 2019). Also, under the context of the aforementioned points, the 1,2,3-triazole nuclei are very common in the corrosion field and become a molecular framework of particular interest in this work. Besides its advantageous structure with three nitrogen

atoms and aromaticity, the synthetic approach via copper-catalyzed azide-alkyne cycloaddition (CuAAC) allows to easily obtain a broad range of substituted triazoles for exploring their role in the corrosion process (Espinoza-Vázquez et al., 2016, Ma et al., 2017, Elazhary et al., 2019, Boutouil et al., 2020, Espinoza Vázquez et al., 2021, Hrimla et al., 2021, Hrimla et al., 2022).

In 2018, Weiwei Zhang and his collaborators (Zhang et al., 2018) investigated three compounds derived from acridine as potential corrosion inhibitors, containing halogenated and non-halogenated substituents, where the first one had better results, maintaining an efficiency range between 92 and 98 % at the maximum concentration of 0.4 mmol/L. In a recent review report, Ekemini D. Akpan and coworkers (Akpan et al., 2022) studied the progress made by acridine derivatives, finding that these heterocyclic compounds with nitrogen atoms are easily synthesized and have low toxicity. Besides, they are easily adsorbed on the surface and form complexes with the surface of the material due to polar groups.

Therefore, the aim of this work is the synthesis and anticorrosive evaluation of three novel 1,2,3-triazolyl-acridine derivatives (Fig. 1) as corrosion inhibitors for carbon steel in an acidic medium (1 mol L^{-1} HCl), using gravimetric techniques and electrochemical measurements, including Electrochemical Impedance Spectroscopy, Linear Polarization Resistance, Potentiodynamic Polarization, and Electrochemical Frequency Modulation. In addition, surface characterization techniques such as atomic force microscopy were employed to further investigate anticorrosive properties. Moreover, the use of first-principles density functional theory (DFT) and Molecular Dynamics were implemented to better understand the interaction and bonding mechanisms of organic molecules with the metal surface, as well as the relationship of different substituents and their efficiencies (Parlak et al., 2022).
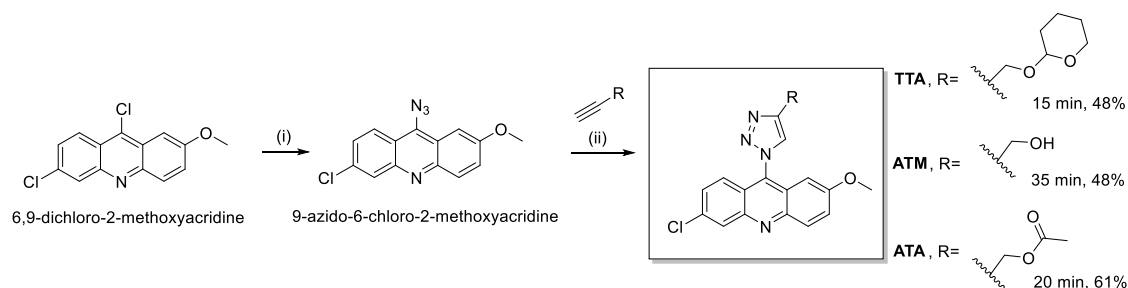
Scheme 1. Synthetic pathway for the synthesis of the new 1,2,3-triazoyl-acridine derivatives. (i) NaN₃, DMF, 65 °C, 42 h. (ii) respective alkyne, CuSO₄·5H₂O, AcOH (cat.), sodium ascorbate, *t*-BuOH/H₂O (1:1), 15–35 min, ultrasound irradiation.

2. Experimental

2.1. Chemical synthesis of the corrosion inhibitors

2.1.1. Materials and equipments

The reagents were purchased from Sigma-Aldrich Brazil and were used without further purification. Column chromatography was performed with silica gel 60 (Merck 70–230 mesh). Analytical thin layer chromatography was performed with silica gel plates (Merck, TLC silica gel 60 F254), and the plates were visualized using UV light. The indicated yields refer to homogeneous materials purified by chromatography and confirmed by spectroscopic techniques. Melting points were obtained on a Thermo Scientific 9100 apparatus. Infrared spectra were collected using KBr pellets on a Perkin-Elmer model 1420 FT-IR spectrophotometer, and the spectra were calibrated relative to the 1601.8 cm^{-1} absorbance of polystyrene. ^{1}H and ^{13}C NMR were recorded at room temperature using a Varian Mercury 300 or Varian Mercury 400 MHz, in the DMSO-d_6. The chemical shift data were reported in units of δ (ppm) downfield from solvent, and the solvent was used as an internal standard; coupling constants (*J*) are reported in hertz and refer to apparent peak multiplicities. High-resolution mass spectra (HRMS) were recorded on a MICROMASS Q-TOF mass spectrometer (Waters). The reactions under ultrasound irradiation were conducted in an UltraSonic Cleaner 750 USC apparatus (UNIQUE).

2.1.2. Methods

At first, in a round bottom flask under nitrogen atmosphere, containing a solution of 6,9-dichloro-2-methoxyacridine (2.0 mmol) in DMF (6.0 mL), sodium azide (6.0 mmol) was added. The reaction was magnetically stirred over 42 h at 65 °C protected from the light (Scheme 1). Thin layer chromatography (TLC) indicated the complete consumption of the reactant. The reaction mixture was poured directly into ice and vacuum filtered. 9-azido-6-chloro-2-methoxyacridine was obtained in quantitative yield as a green solid and used in the next reaction step without further purification. **FTIR ν_{max} (cm^{-1}):** 2108, 1633, 1556, 1518, 1475, 1248, 1215, 1029, 914, 819, 658.

Then, to a round bottom flask, a mixture of 9-azido-6-chloro-2-methoxyacridine (1.00 mmol), respective alkyne (1.20 mmol), CuSO$_4$·5H$_2$O (0.072 mmol), an excess of sodium ascorbate (0.16 mmol), acetic acid (0.33 mmol, 30 mol% based on the azido compound) and a mixture of an equal amount of *tert*-butanol and water (1.00 mL) was subjected to ultrasound irradiation for 15–35 min protected from the light (Scheme 1). The reactions were monitored by TLC. After, a liquid–liquid extraction was performed with ethyl acetate and water. The organic layer was dried with anhydrous sodium sulphate, filtered off and the solvent removed by reduced pressure evaporation. The resultant mixture was purified by column chromatography using a gradient of hexanes/ethyl acetate or chloroform/ethyl acetate, depending on the polarity of each compound, obtaining compounds TTA, ATM and ATA.

2.1.2.1. 6-chloro-2-methoxy-9-(4-(((tetrahydrofuran-3-il)oxy)methyl)-1H-1,2,3-triazol-1-il)acridine (TTA). 15 min. Yellow solid, 48 % **m.p.:** 170.2–171.4 °C. **FTIR ν_{max} (cm^{-1}):** 3087, 2940, 2869, 1631, 1474, 1447, 1423, 1222, 1202, 1120, 1063, 1031, 970, 935, 905, 896, 872, 824, 813, 791, 775, 571. **^{1}H NMR (300.00 MHz, DMSO-d_6) δ (ppm):** 1.46–1.59 (m, 4H), 1.60–1.90 (m, 2H), 3.53 (dd, *J* = 5.7 and 11.0 Hz, 1H), 3.80 (s, 3H), 4.81–4.98 (m, 4H), 6.52 (d, *J* = 2.3 Hz, 1H), 7.37 (d, *J* = 9.4 Hz, 1H), 7.69 (ddd, *J* = 2.3, 3.9 and 9.4, Hz, 2H), 8.23 (d, *J* = 9.4 Hz, 1H), 8.34 (d, *J* = 2.3 Hz, 1H), 8.81 (s, 1H). **^{13}C NMR (APT, 75.0 MHz, DMSO-d_6) δ (ppm):** 18.9, 20.2, 24.9, 25.0, 30.1, 54.9, 55.5, 55.6, 59.5, 61.4, 62.5, 93.3, 97.3, 97.5, 97.7, 120.5, 122.9, 124.0, 126.7, 127.4, 127.8, 129.0, 129.1, 131.2, 134.6, 135.6, 144.9, 146.5, 146.8, 148.7, 158.7. **HRMS** (ESI) calc for C$_{22}$H$_{21}$ClN$_4$NaO$_3$ [M + Na]$^+$: 447.119439 Found. 447.118728. Δ −1.6 ppm.

2.1.2.2. (1-(6-chloro-2-methoxyacridin-9-il)-1H-1,2,3-triazol-4-il)methanol (ATM). 35 min. Green solid, 48 %. **m.p:** 207.1–209.3 °C. **FTIR ν_{max} (cm^{-1}):** 3234, 3162, 1628, 1566, 1481, 1440, 1424, 1305, 1289, 1234, 1223, 1204, 1070, 1046, 1038, 1014, 938, 836, 818, 712. **^{1}H NMR (500.00 MHz, DMSO-d_6) δ (ppm):** 3.80 (s, 3H), 4.80 (d, *J* = 5.6 Hz, 2H), 5.35 (d, *J* = 5.6 Hz, 1H), 6.55 (d, *J* = 2.3 Hz, 1H), 7.34 (d, *J* = 9.3 Hz, 1H), 7.67–7.70 (m, 2H), 8.22 ppm (d, *J* = 9.3 Hz, 1H), 8.33 (d, *J* = 2.3 Hz, 1H), 8.67 (s, 1H). **^{13}C NMR (APT, 125.00 MHz, DMSO-d_6) δ (ppm):** 55.52, 56.12, 98.20, 121.07, 123.48, 124.53, 127.17, 127.28, 127.98, 129.55, 131.67, 135.06, 136.30, 147.04, 147.29, 149.30, 159.2. **HRMS** (ESI) calc for C$_{17}$H$_{14}$ClN$_4$O$_2$ [M + H]$^+$: 341.079980 Found. 341.080311. Δ + 1.0 ppm.

2.1.2.3. (1-(6-chloro-2-methoxyacridin-9-il)-1H-1,2,3-triazol-4-il)methyl acetate (ATA). 20 min. Green solid, 61 %. **m.p.:** 155.4–155.0 °C. **FTIR ν_{max} (cm^{-1}):** 3438, 3088, 3068, 2961, 1736, 1633, 1476, 1463, 1447, 1437, 1424, 1385, 1366, 1276, 1256. **^{1}H NMR (500.0 MHz, DMSO-d_6) δ (ppm):** 2.12 (s, 3H), 3.80 (s, 3H), 5.40 (s, 2H), 6.48 (d, *J* = 2.2 Hz, 1H), 7.36 (d, *J* = 9.4 Hz, 1H), 7.68 (td, *J* = 2.2 and 9.4 Hz, 2H), 8.22 (d, *J* = 9.4 Hz, 1H), 8.33 (d, *J* = 2.2 Hz, 1H), 8.86 (s, 1H). **^{13}C NMR (APT, 125.00 MHz, DMSO-d_6) δ (ppm):** 20.55, 55.52, 56.95, 97.43, 120.35, 122.81, 123.91, 126.67, 127.44, 128.53, 129.13, 131.14, 134.54, 135.27, 142.89, 146.46, 146.70, 158.72, 170.06. **HRMS** (ESI) calc for C$_{19}$H$_{16}$ClN$_4$O$_3$ [M + H]$^+$: 383.09054 Found. 383.091637. Δ −2.9 ppm.

2.2. Materials

Hydrochloric acid solution (1 mol/L) was produced via dilution of HCl 37 % (analytical grade) in ultrapure H$_2$O. 1020 Mild Steel with the following composition (Table 1) was used in this work:

The metal specimens used in the gravimetric experiments had an exposed around 3.5 cm^2 and the working electrode area was limited in 1 cm^2.

2.3. Gravimetric experiments

The Weight Loss Study (WLS) was conducted in accordance to the norms of the American Society for Testing Material (ASTM G1-03 (2017)) (Faydy et al., 2019). The immersion time of 5 h was determined when the corrosion rate of the black solution started to become stable (different immersion times were applied, from 0.5 h to 10 h). WLS was performed at three temperatures (298, 318 and 338 K). The data was used to determine the corrosion rate and the anticorrosive efficiencies of the tested compounds (de Sampaio et al., 2020).

2.4. Electrochemistry

Electrochemical measurements were performed in a three-electrode cell. Mild steel was the working electrode, a long platinum wire was the counter electrode, and for the reference electrode Ag|AgCl was used. The instrument was an AutoLab PGSTAT 128 N (Metrohm®). Open Circuit Potential was measured for 60 min before each sequence of experiments (Fernandes et al., 2022a, 2022b). They were:

- Electrochemical Frequency Modulation (EFM, with a base frequency of 0.1 Hz, applied multipliers of 2 and 5, and 10 mV amplitude) (Machado Fernandes et al., 2023);

Table 1
1020 Mild Steel composition.

Element	C	S	P	Si	Mn	Fe
%	0.21	0.08	0.03	0.02	0.58	Balance

Table 2

Weigh Loss Study for mild steel in the absence and presence of different concentrations of TTA, ATM, and ATA in 1 mol/L HCl at 298, 318 and 338 K.

Temperature (K)		298 K		318 K		338 K	
Compound	Conc. (mmol/L)	CR (mm year^{-1})	η (%)	CR (mm year^{-1})	η (%)	CR (mm year^{-1})	η (%)
Blank	–	1.713 ± 0.037	–	9.831 ± 0.269	–	49.168 ± 0.856	–
TTA	0.0625	0.615 ± 0.007	64.1	3.093 ± 0.243	68.5	12.904 ± 0.596	73.8
	0.125	0.522 ± 0.054	69.5	2.504 ± 0.165	74.2	10.499 ± 0.821	78.6
	0.25	0.436 ± 0.044	74.5	2.060 ± 0.208	79.0	8.641 ± 1.132	82.4
	0.50	0.317 ± 0.058	81.5	1.617 ± 0.133	83.6	6.959 ± 1.062	85.8
	1.00	0.254 ± 0.012	85.2	1.131 ± 0.102	88.5	4.725 ± 0.348	90.4
ATM	0.0625	0.583 ± 0.043	66.0	2.913 ± 0.158	70.4	11.390 ± 0.286	76.8
	0.125	0.490 ± 0.022	71.4	2.186 ± 0.336	77.8	8.635 ± 0.729	82.4
	0.25	0.390 ± 0.043	77.2	1.823 ± 0.215	81.5	6.914 ± 0.555	85.9
	0.50	0.289 ± 0.064	83.1	1.463 ± 0.263	85.1	4.410 ± 0.315	91.0
	1.00	0.164 ± 0.023	90.4	0.837 ± 0.136	91.5	3.116 ± 0.146	93.7
ATA	0.0625	0.496 ± 0.022	71.1	2.393 ± 0.116	75.7	9.378 ± 0.653	80.9
	0.125	0.383 ± 0.058	77.6	1.893 ± 0.112	80.7	8.023 ± 0.886	83.7
	0.25	0.308 ± 0.017	82.0	1.496 ± 0.197	84.8	6.348 ± 0.663	87.1
	0.50	0.220 ± 0.022	87.2	1.175 ± 0.132	88.0	4.243 ± 0.113	91.4
	1.00	0.100 ± 0.026	94.2	0.492 ± 0.182	95.0	1.796 ± 0.222	96.4

- Electrochemical Impedance Spectroscopy (EIS, with a frequency range of 100000–0.1 Hz and 10 mV amplitude) (Fernandes et al., 2019a, 2019b, 2019c);
- Linear Polarization Resistance (LPR, potential range of ± 10 mV and 0.075 mV s^{-1}) (Machado Fernandes et al., 2020a, 2020b);
- Potentiodynamic Polarization (PP, potential range of ± 300 mV and 1 mV s^{-1}) (Fernandes et al., 2019a, 2019b, 2019c).

2.5. Atomic force Microscopy (AFM)

The topography of the mild steel surface was analyzed after the gravimetric experiment on corroded and inhibited scenarios, and also after the grounding process, with the help of a Nanosurf Easy Scan 2 Atomic Microscope.

2.6. First-principles DFT simulation

The first-principles DFT method is a wonderful theoretical tool in predicting structural and electronic properties. Herein, the inhibitor-iron interactions were fully optimized by spin polarized first-principles DFT, including dispersion interaction (DFT-D3) and ultra-soft pseudo-potentials using the CASTEP code (Clark et al., 2005). The generalized gradient approximation (GGA) within its PBE formulation was used for the electron exchange and correlation (Perdew et al., 1996). The adsorption systems were fully optimized using a self-consistent field (SCF) tolerance of 10^{-6} eV/atom, and plane-wave basis set with an energy cut-off of 30 Ry. All other convergence tolerance values were set according to fine quality. Meanwhile, the bulk lattice parameters optimization was carried out using (8x8x8) k-point grid, which was reduced to (2x2x1) k-point grid for adsorption models.

The optimization of bulk lattice parameters reproduced a value of 2.854 Å, which is close to the experimental one of 2.862 Å, confirming the accuracy of selected parameters. Inhibitor-iron adsorption models were generated by constructing Fe(110) iron surface consisting of a (5x5) supercell and a vacuum spacing of 20 Å along the z-direction separating periodic image in each direction. Then, inhibitor molecules were placed on the top side of the slab and all atoms were allowed to relax except the two bottom-most atomic layers. DFT optimization of standalone molecules was carried out by constructing a cubic box of 30 Å in size. The interaction energy was used as a main parameter to estimate the adsorption strength of molecules, which is calculated according to the following equation:

$$E_{\text{inter}} = E_{\text{mol/surf}} - \left(E_{\text{mol}} + E_{\text{surf}} \right) \qquad (1)$$

where E_{mol}, E_{surf}, and $E_{\text{mol/surf}}$ denote the total energies of isolated molecules, Fe(110) iron surface, and molecule/Fe(110) adsorption systems.

2.7. Molecular dynamics simulation

Molecular dynamics simulation can be used to get information about how strong the interaction of inhibitor molecules with the iron surface in presence of a simulated solution is (Obot et al., 2018). To this end, an iron surface was constructed from (110)-cleaved iron unit cell, extended to (7x7) supercell and then placed in contact with a solvent layer consisting of one inhibitor molecule, 491 water molecules, 9 H_3O^+ and 9Cl$^-$. After initial optimization of constructed simulation boxes via Smart Minimizer protocol, MD equilibrium process was carried out for 5000 ps in canonical ensemble (NVT) using COMPASSIII force field (Sun, 1998). Furthermore, the summations techniques of Ewald and atom-based cut-off were used to treat non-bonded electrostatic and van der Waals interactions, respectively. The velocity Verlet integration scheme using a time step of 1 fs was used to solve the motion equation of Newton (Swope et al., 1982). The temperature was controlled by Nose-Hoover thermostat (Martyna et al., 1992). Because of its known over-estimation of the interaction energy magnitudes, interaction energy values will not be analyzed from MD simulations.

3. Results and discussion

3.1. Synthesis of the new corrosion inhibitors

The novel 1,2,3-triazoyl-acridine derivatives were obtained through a simple two step-approach, as outlined in the Scheme 1. The first step involved a nucleophilic aromatic substitution reaction between the commercially available 6,9-dichloro-2-methoxyacridine and sodium azide, providing the intermediate 9-azido-6-chloro-2-methoxyacridine, as a green solid, in quantitative yield. This azide intermediate was readily reacted with the corresponding commercially available alkyne under an ultrasound-assisted CuAAC methodology, as previously described for the isatine-triazole derivatives preparation (Silva et al., 2016), furnishing TTA, ATM, and ATA after 15–35 min, in 48–61 % yield range.

The insertion of the azide group in the intermediate 9-azido-6-chloro-2-methoxyacridine was confirmed through FT-IR spectroscopy. A strong absorption band at 2108 cm^{-1} corresponding to the characteristic stretching N = N = N bond was observed (Figure S1, supplementary information). The structures of all 1,2,3-triazoloyl-acridine derivatives were fully characterized through spectroscopic and spectrometric analyses (Figures S2-S13, supplementary information). All ^{1}H

NMR spectra showed the characteristic singlet of the hydrogen atom of triazolic ring CH at 8.81, 8.67, and 8.86 ppm for TTA, ATM, and ATA respectively, confirming the 1,2,3-triazolic nucleus formation. The other observed ^{1}H NMR signals and all ^{13}C NMR signals were also in good agreement with the expected structures for the desired compounds. Moreover, HRMS unequivocally confirmed the molecular structures of the desired corrosion inhibitors.

3.2. Weight Loss Study

Gravimetric experiments are a reliable tool in the corrosion inhibitor field. WLS is applied to determine whether a particular compound acts attenuating the metallic in an aggressive environment, allowing the calculation of the corrosion rate (CR) through the mass variation of the specimens. The difference in the CR values permits obtaining anticorrosive efficiency and surface coverage value (Chaouiki et al., 2022). All data is shown in Table 2 for an immersion time of five hours:

The results show that all three molecules at the lowest evaluated concentration (0.0625 mmol/L) already act very satisfactorily as corrosion inhibitors, presenting from 64 to 71 % efficiency. That is a great result since usually, at this low concentration, organic compounds do not present relevant corrosive inhibitory activity (Cherrad et al., 2022) with exceptions being reported in the literature (Noor and Al-Moubaraki, 2008).

All three compounds have different substituents attached to the triazolic nucleus. TTA has a 2-methoxytetrahydro-2*H*-pyran (tetrahydropyranyl ether), ATM has a methanol (methyl ether) and ATA has a methyl acetate (an acetate). Those different structures clearly influence the anticorrosive efficiency of the 1,2,3-triazolyl-acridine derivatives. The presence of a 6-member saturated heterocycle leads to a result of 85.2 % corrosion mitigation for TTA, diminishing the corrosion rate (CR) from 1.713 to 0.254 mm year^{-1}. When we exchange this substituent for one with less steric effect as –CH$_2$-OH, the efficiency goes up to 90.4 %, lowering CR to 0.164 mm year^{-1}. Changing now for another one with a similar steric effect but with a higher electron density due to the presence of another O atom (acetate) and a π bond, a better anticorrosive efficiency is found, reaching 94.2 %, with the corrosion rate going from 1.713 to 0.100 mm year^{-1}. Those values were reached at 1.00 mmol/L and prove the three 1,2,3-triazolyl-acridine derivatives are great corrosion inhibitors for mild steel in acidic media. So, the tested compounds follow the following order of inhibition: ATA > ATM > TTA.

The anticorrosive efficiency of organic compounds is directly related to their capacity of interacting with metallic alloy and adsorb on the surface, producing a protective layer that will prevent the corrosion process to take place. Thus, the literature well characterizes the fact that this protection is precisely the surface area covered by organic compounds. With that in mind, evidencing that the different substituents present in the evaluated compounds directly influence the anticorrosive efficiency of the 1,2,3-triazolyl-acridine derivatives, we made use of theoretical studies (*vide infra*) to understand their influence on the electronic properties of the compounds and how they interact with the mild steel surface.

3.2.1. Influence of temperature

It is important for corrosion inhibitors to maintain good levels of efficiency at higher temperatures since many real-life applications of hydrochloric acid do not take place at room temperature (Bashir et al., 2020). Considering that, gravimetric experiments were also performed at 318 and 338 K and the results are exhibited in Table 2.

The corrosive process exhibits an endothermic nature; thus, as the temperature increases, the corrosion rate of 1020 mild steel in hydrochloric acid intensifies. Specifically, at temperatures of 298 K, 318 K, and 338 K, the corrosion rates escalate from 1.713 mm/year to 9.831 mm/year and further to 49.168 mm year^{-1}, respectively (Fernandes et al., 2020).

The three evaluated compounds presented better efficiencies at low,

Table 3
Adsorption results for TTA, ATM, and ATA at 298, 318, and 338 K.

Compound	Temperature (K)	R^2	K_{ads} (L/mol)	ΔG_{ads} (kJ/mol)	ΔH_{ads} (kJ/mol)	ΔS_{ads} (J K^{-1} mol^{-1})
TTA	298	0.9994	26253.6	−35.2	8.1	
	318	0.9992	30450.7	−37.9		145.0
	338	0.9994	38925.6	−41.0		
ATM	298	0.9981	22583.6	−34.8	14.4	
	318	0.9986	30759.8	−37.9		165.0
	338	0.9998	45829.5	−41.4		
ATA	298	0.9984	27434.8	−35.3	8.7	
	318	0.9984	33145.5	−38.1		147.5
	338	0.9991	41493.8	−41.2		

mid, and high concentrations at both higher temperatures tested. TTA increased its anticorrosive mitigation from 64.1 to 85.2 % to 68.5–88.5 % (at 318 K) and to 73.8–90.4 % (at 338 K), enhancing 7 and 15 % at the lowest concentration (0.0625 mmol/L) and 4 and 6 % at the highest concentration (1.00 mmol/L). ATM showed improvements of 8 and 16 % in its corrosion inhibitions efficiency at the lowest concentration. And at the highest, this OCI went from 90.4 to 91.5 (at 318 K) to 93.7 % (at 338 K), presenting excellent results.

ATA was the best corrosion inhibitor for mild steel in acidic media at room temperature. And those results were even better at elevated temperatures. For starters, at 318 K, an expressive 75 % efficiency was achieved at the lowest concentration tested. At 1.00 mmol/L, the drop-in corrosion rate was from 9.831 to 0.492 mm year^{-1}, resulting in an emphatic 95 % anticorrosive efficiency. At 338 K, for 0.0625 mmol/L there is a corrosion mitigation greater than four-fifths of the corrosion rate of the blank solution (from 49.168 to 9.378 mm year^{-1}). And at the highest concentration, ATA achieved exceptional results, surpassing 96 % of anticorrosive efficiency, proving to be an excellent corrosion inhibitor for mild steel in 1 mol/L HCl at room and high temperatures.

The observed sequence ATA > ATM > TTA at elevated temperatures (318 and 338 K) aligns with the pattern observed previously (298 K), confirming these findings. The enhanced anticorrosive efficiency of organic molecules at higher temperatures suggests that chemisorption is the primary mode of interaction between these compounds and the mild steel surface. This interaction becomes more prominent and robust as the temperature increases, indicating a strong correlation between temperature and the strengthening of the chemisorptive bonds.

With the indication that adsorption of the studied inhibitors is mainly governed by chemisorption, we applied the Arrhenius equation to calculate the apparent activation energy (E$_a$). The corresponding results are presented in Table S1. The obtained activation energy (Ea) values for TTA, ATM, and ATA at concentrations of 0.0625, 0.125, 0.250, 0.500, and 1.000 mmol/L fell within the range of 57.2 to 63.7 kJ mol^{-1}, in contrast to the 70.2 kJ mol − 1 observed for the blank solution. The lower activation energy values in the presence of organic corrosion inhibitors compared to the blank solution indicate a chemisorption process, confirming the earlier discussion (Popova et al., 2003, Noor and Al-Moubaraki, 2008).

3.3. Adsorption Isotherm

Eleven different isotherms (Freundlich, Frumkin, Langmuir, Temkin, Dubinin–Radushkevic, Kiselev, Flory-Huggins, Hill-De Boer, Elovich, Halsey, and Fowler–Guggenheim) were tested using their mathematical equation to understand more about the adsorption process. Each on has its own theory and the evaluation criterion for choosing the best fitting via coefficient of determination (R^2) (En-Nylly et al., 2023).

TTA, ATM, and ATA suited the Langmuir monolayer formation theory at all tested temperatures (298, 318, 338 K). This means that each molecule adsorbs on one specific active site of the mild steel surface and do not interact with neighboring compounds (Jiang et al., 2023).
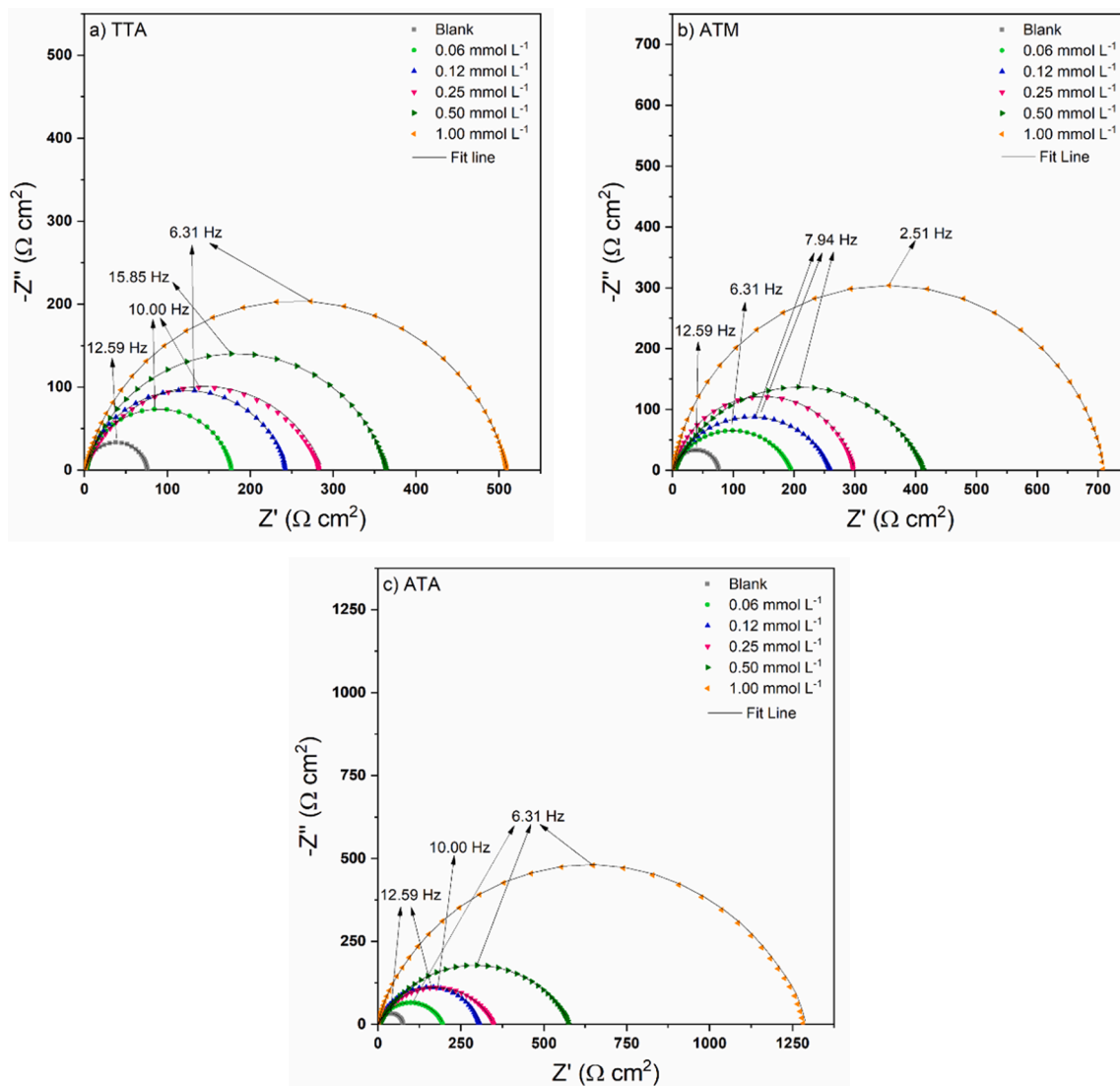
Fig. 2. Nyquist plots for TTA, ATM, and ATA in 1.00 mol/L HCl at 298 K.

Fig. S14 shows the graphs for all three OCIs, making it possible to calculate the adsorption constant (K_{ads}) using the Langmuir equation:

$$\frac{C}{\theta} = \frac{1}{K_{ads}} + C \tag{1}$$

The high K_{ads} values obtained (Table 3) for all three compounds display that the equilibrium is dislocated favoring the adsorption of TTA, ATM, and ATA on the mild steel surface, dislocating water molecules. The Gibbs adsorption energy (ΔG_{ads}) was then calculated according to the following equation (Liu et al., 2023):

$$\Delta G_{ads} = -R \times T \times \ln(55.5 \times K_{ads}) \tag{2}$$

It is well known in the literature that ΔG_{ads} values less negative than -20 kJ mol^{-1} characterize physisorption processes, while ΔG_{ads} values more negative than -40 kJ mol^{-1} characterize chemisorption processes. From the values exhibited in Table 3, it is possible to realize that TTA, ATM, and ATA experience both interaction types in the adsorption process on the mild steel surface (Hajjaji et al., 2021).

The variation of adsorption enthalpy was also calculated, using ΔG_{ads} vs. T(K). As shown in Table 3, it was found that for TTA, ATM, and ATA, those values are positive, characterizing an endothermic process, supporting the chemisorption phenomenon.
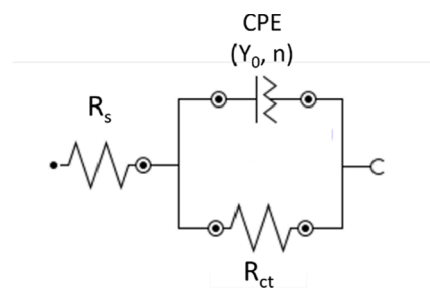

Fig. 3. Equivalent circuit used to simulate Electrochemical Impedance Spectroscopy results.

3.4. Electrochemical Impedance Spectroscopy

The technique Electrochemical Impedance Spectroscopy (EIS) allowed to better understand the phenomena occurring in the electrolyte/metal interface, giving details about the protection mechanism. The Nyquist plots for TTA, ATM, and ATA is shown in Fig. 2.

Due to the square axes in the Nyquist plots, it is possible to observe from Fig. 2 that the results are depressed non-perfect semicircles, resulting in frequency dispersion. The graphs also exhibit a single loop

Table 4
EIS data for TTA, ATM, and ATA in 1.00 mol/L HCl at 298 K.

Compound	Conc. (mmol/L)	R_s (Ω cm^2)	CPE		C_{dl} (μF cm^{-2})	R_{ct} (Ω cm^2)	η (%)	χ^2 (x 10^{-4})
			Y_0 ($\mu\Omega^{-1}$S^{n}cm^{-2})	n				
Blank	–	1.3 ± 0.2	149.0 ± 10.0	0.923 ± 0.006	72.9	75.0 ± 4.1	0.0	1.8
TTA	0.0625	1.5 ± 0.3	96.5 ± 6.2	0.884 ± 0.005	30.7	183.2 ± 15.0	59.1	4.6
	0.125	1.0 ± 0.4	111.0 ± 8.8	0.868 ± 0.008	27.8	243.5 ± 12.8	69.2	7.7
	0.25	1.6 ± 0.1	130.2 ± 14.1	0.832 ± 0.002	23.5	283.2 ± 19.1	73.5	3.2
	0.50	0.9 ± 0.5	107.7 ± 10.5	0.838 ± 0.004	18.0	363.4 ± 22.6	79.4	2.5
	1.00	1.2 ± 0.2	95.3 ± 4.4	0.826 ± 0.004	14.1	509.3 ± 25.4	85.3	4.8
ATM	0.0625	0.5 ± 0.1	168.0 ± 18.2	0.842 ± 0.005	28.9	195.0 ± 15.6	61.5	5.0
	0.125	1.0 ± 0.4	117.0 ± 3.6	0.860 ± 0.008	26.8	252.8 ± 23.9	70.3	5.2
	0.25	1.0 ± 0.6	108.0 ± 7.4	0.847 ± 0.010	20.7	301.6 ± 20.0	75.1	4.9
	0.50	1.5 ± 0.3	81.8 ± 8.0	0.847 ± 0.003	16.1	412.4 ± 29.8	81.8	3.8
	1.00	0.9 ± 0.3	72.5 ± 5.1	0.832 ± 0.004	10.4	708.1 ± 33.6	89.4	2.3
ATA	0.0625	1.2 ± 0.1	159.4 ± 8.1	0.832 ± 0.012	28.3	244.7 ± 20.8	69.4	6.1
	0.125	1.4 ± 0.4	153.1 ± 12.9	0.817 ± 0.009	23.0	310.6 ± 31.3	75.8	4.0
	0.25	0.9 ± 0.1	88.3 ± 6.5	0.854 ± 0.003	17.6	360.2 ± 35.9	79.2	3.1
	0.50	1.8 ± 0.6	77.8 ± 7.1	0.836 ± 0.005	13.6	577.0 ± 51.4	87.0	2.9
	1.00	1.0 ± 0.5	50.9 ± 2.3	0.831 ± 0.001	6.8	1279.5 ± 77.7	94.1	2.6
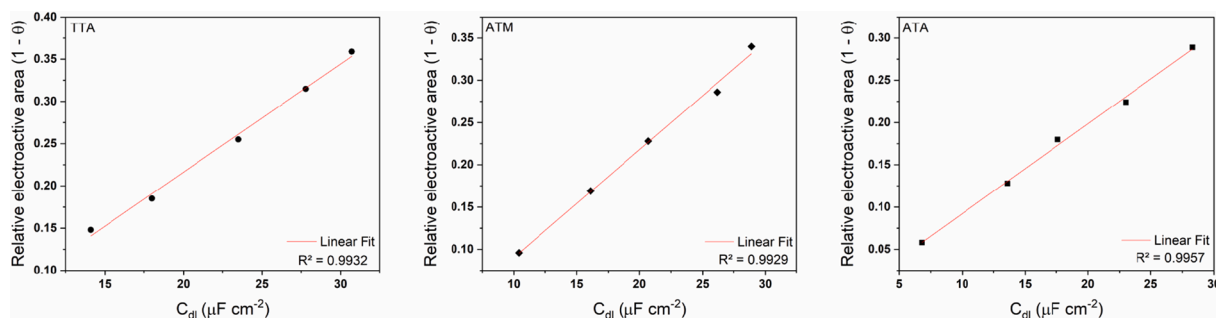
Fig. 4. Plots of double layer capacitance vs relative electroactive area for TTA, ATM, and ATA in 1 mol/L HCl.

form, indicating the presence of only one capacitive phase (Olasunkanmi et al., 2020).

To translate those results to numbers, an equivalent circuit was employed (Machado Fernandes et al., 2020a, 2020b, AlSalhi et al., 2023, Andrés Coy-Barrera et al., 2023). The system is composed by a solution resistance (R_s), a charge transfer resistance (R_{ct}) and a constant phase element (CPE), organized as presented in Fig. 3. It is important to mention that CPE was used instead of a pure capacitor due to surface roughness and inhomogeneity, leading to the depressed form observe in the Nyquist plots (Fernandes et al., 2022a, 2022b).

The obtained data is present in Table 4. The values of n prove that CPE was corrected used and the working electrode is not a pure capacitor (n = 1) and suffers from surface inhomogeneity. Also, Brug's formula (Brug et al., 1984) (Eq. 3) was used to calculate the double layer capacitance (C_{dl}). This equation is used when slow charge transfer rules the corrosive process, which can be inferred by the single loop in the Nyquist plots in both blank and inhibited solutions.

$$C_{dl} = Y_0^{1/n} \times \left(\frac{1}{R_s} + \frac{1}{R_{ct}} \right)^{(n-1)/n} \quad (3)$$

Using the Helmholtz equation, the double layer capacitance can be defined as follow:

$$C_{dl} = \frac{\varepsilon^0 \times \varepsilon \times S}{d} \quad (4)$$

The term ε^0 is always constant, as it represents the air permittivity. The other terms are local dielectric constant (ε), surface in contact with the electrolyte (S), and layer thickness (d). Thus, when introducing organic molecules into the aggressive medium and they adsorb on the metal surface to protect the metal from the corrosive process, the

displacement of water molecules from the working electrode surface occurs, significantly decreasing the local dielectric constant and the exposed metallic surface and increasing the thickness of the protective layer, explaining the difference in C_{dl} values from blank and inhibited solutions (Rbaa and Lakhrissi, 2019).

To go deep and understand more about the change in C_{dl} values when varying the concentration of the three inhibitors, we made use of a crossing data between those results and the weight loss results, as first proposed by Fernandes et al (Fernandes et al., 2019a, 2019b, 2019c). So, a graph is suggested plotting the double layer capacitance versus what is called relative electroactive area, e.g., the surface not covered by organic molecules (the S from the Helmholtz equation but replaced for 1 – θ obtained via gravimetric experiments), as shown in Fig. 4.

It can be seen from Fig. 4 and the presented coefficient of determination that an excellent linear fit is found for the three compounds, which suggests that the fraction ε/d is constant, corroborating the Langmuir theory seen in section 3.3. of a protective monolayer formation on the metallic surface (Machado Fernandes et al., 2022a, 2022b).

The Nyquist plots (Fig. 2) showed bigger semicircles as TTA, ATM, and ATA concentration in the electrolyte increased. Such diameters are associated with charge transfer resistance, illustrating the difficulty of occurring redox reactions at the working electrode (Damej et al., 2021, Al Jahdaly, 2023). The results exhibited in Table 4, after the simulation with the equivalent circuit, confirm that idea.

TTA reaches a R_{ct} of 509.3 Ω cm^2 at 1.00 mmol/L (in comparison to 75.0 Ω cm^2 from the blank solution) giving more than 85 % anticorrosive efficiency. ATM present 89.4 % efficiency mitigating corrosion (R_{ct} of 708.1 vs 75.0 Ω cm^2 from the blank solution) at the highest concentration tested. ATA prevents the 1020 mild steel corrosion in a range from 69 to 94 %, with Rct values varying from 244.7 to 1279.5 Ω cm^2.

Table 5
PP and LPR data for TTA, ATM, and ATA in 1.00 mol/L HCl at 298 K.

Compound	Concentration (mmol/L)	E_{corr} (V)	R_p (Ω cm^2)	η (%)
Blank	–	-0.457 ± 0.004	78.8 ± 5.4	–
TTA	0.0625	-0.461 ± 0.002	203.5 ± 11.6	61.3
	0.125	-0.456 ± 0.004	258.5 ± 14.8	69.5
	0.25	-0.460 ± 0.003	305.4 ± 25.9	74.2
	0.50	-0.455 ± 0.001	392.9 ± 20.6	79.9
	1.00	-0.453 ± 0.003	554.2 ± 30.0	85.8
ATM	0.0625	-0.476 ± 0.006	207.4 ± 8.8	62.0
	0.125	-0.467 ± 0.005	261.5 ± 6.3	70.0
	0.25	-0.461 ± 0.001	303.7 ± 18.1	74.0
	0.50	-0.455 ± 0.002	439.7 ± 29.2	82.2
	1.00	-0.440 ± 0.002	788.0 ± 44.4	90.0
ATA	0.0625	-0.464 ± 0.003	260.9 ± 11.0	69.8
	0.125	-0.467 ± 0.001	325.1 ± 18.5	75.8
	0.25	-0.465 ± 0.005	377.9 ± 26.7	79.2
	0.50	-0.464 ± 0.004	609.6 ± 49.8	87.1
	1.00	-0.480 ± 0.004	1271.0 ± 88.9	93.8

These results corroborate the gravimetric ones and prove that all three compounds are excellent corrosion inhibitors.

3.5. Linear Polarization resistance

Linear Polarization Resistance (LPR) experiments were used to acquire the polarization resistance (R_p) of the mild steel working electrode. By varying the potential (± 10 mV vs OCP) and collecting the current resulting from this disturbance in the system, R_p is obtained through Ohm's Law (Fernandes et al., 2020, Altunbaş Şahin, 2022).

From the results in Table 5, it is possible to realize that even at the lowest tested concentration (0.06 mmol/L), all three organic compounds prevent the oxidation from the working electrode at satisfactory levels (between 60 and 70 % efficiency). At 1.00 mmol L^{-1}, TTA, ATM, and ATA present 554.2, 788.0, and 1271.0 Ω cm^2, reaching 85.8, 90.0, and 93.8 % anticorrosive efficiency, respectively, in agreement with EIS data.

3.6. Potentiodynamic Polarization

The polarization curves were acquired after an extensive potential sweep of $\pm$ 300 mV and are exhibited in Fig. 5. It is possible to observe that in all three cases, the presence of the organic compound in the electrolyte affects both cathodic and anodic currents (Kaskah et al., 2017). And the decay in corrosion current density is more conspicuous as the concentration of inhibitor increases, directly influencing in the two redox reactions: hydrogen gas evolution and iron dissolution (Rbaa et al., 2020).

It is well defined in the literature that changes in corrosion potential (E_{corr}) inside the range of $\pm$ 85 mV characterize organic molecules as mixed-type, affecting both cathodic and anodic branches (Fernandes et al., 2019a, 2019b, 2019c, Nahlé et al., 2022, Zaher et al., 2022). The results of E_{corr} are shown in Table 5 and prove that TTA, ATM, and ATA are mixed-type corrosion inhibitors for 1020 mild steel in 1.00 mol/L HCl at 298 K.

A crucial observation to note is that when potentials within the range of 0.250 V (vs Ag|AgCl) are approached, the effectiveness of the three inhibitors against corrosion significantly diminishes. This phenomenon can be attributed to the region's characterization as the desorption potential. It is plausible to infer that in this range, the rate of desorption surpasses the rate of adsorption, leading to accelerated metal dissolution and subsequently heightened corrosion current density (Mourya et al., 2014, Zulkifli et al., 2017).
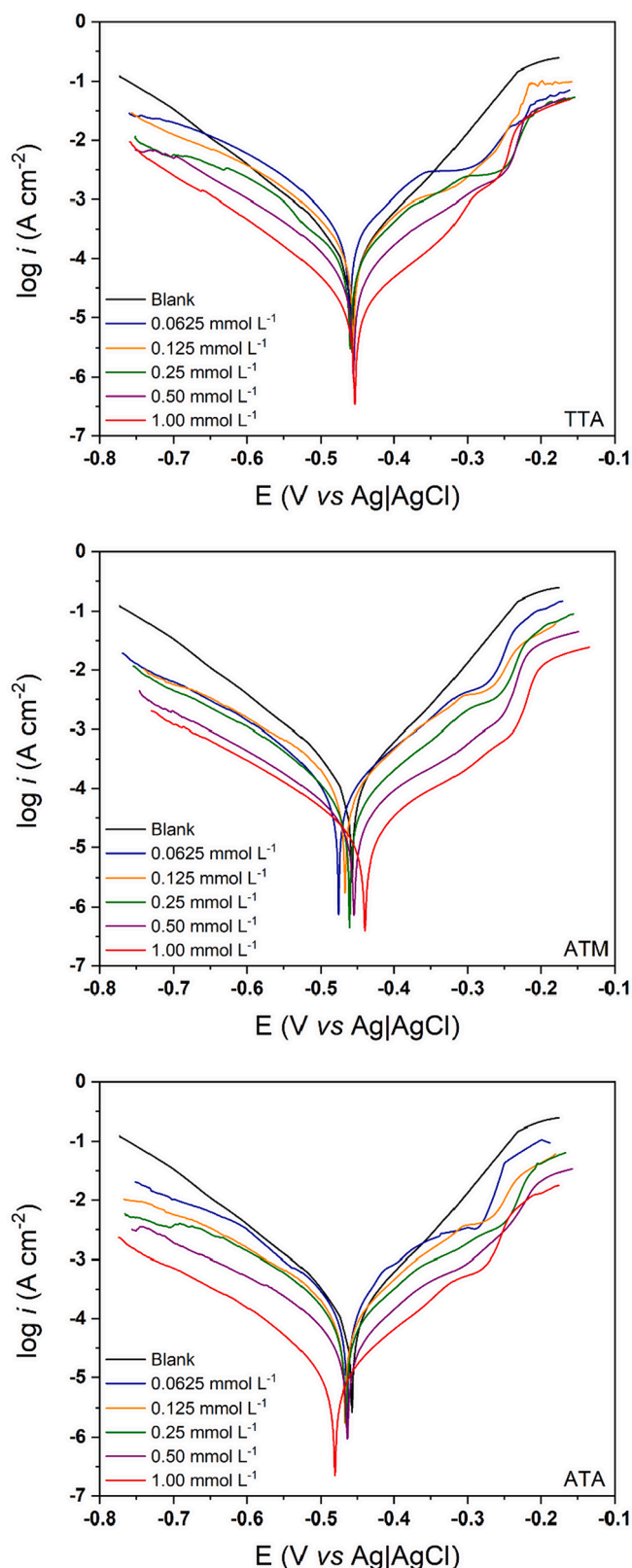

Fig. 5. Potentiodynamic Polarization curves for TTA, ATM, and ATA in 1.00 mol/L HCl at 298 K.

3.7. Electrochemical Frequency Modulation

Electrochemical Frequency Modulation (EFM) technique was employed to collect the values of corrosion current density (i_{corr})

Table 6
EFM data for TTA, ATM, and ATA in 1.00 mol/L HCl at 298 K.

Compound	Conc. (mmol/L)	CF-2	CF-3	βa (V dec^{-1})	-βc (V dec^{-1})	i_{corr} (μA cm^{-2})	η (%)
Blank	–	1.79 ± 0.05	3.20 ± 0.03	0.0462 ± 0.0002	0.0514 ± 0.0004	120.1 ± 10.4	–
TTA	0.0625	1.85 ± 0.03	2.69 ± 0.02	0.0450 ± 0.0003	0.0516 ± 0.0005	45.4 ± 4.8	62.5
	0.125	1.71 ± 0.08	2.76 ± 0.06	0.0400 ± 0.0005	0.0541 ± 0.0003	36.1 ± 5.9	70.0
	0.25	1.99 ± 0.06	3.25 ± 0.05	0.0461 ± 0.0001	0.0489 ± 0.0002	30.4 ± 3.1	74.8
	0.50	1.93 ± 0.02	3.02 ± 0.05	0.0470 ± 0.0004	0.0498 ± 0.0004	23.5 ± 3.0	80.5
	1.00	1.84 ± 0.03	2.75 ± 0.01	0.0451 ± 0.0002	0.0506 ± 0.0003	17.5 ± 1.6	85.5
ATM	0.0625	1.86 ± 0.02	2.69 ± 0.03	0.0416 ± 0.0004	0.0471 ± 0.0006	40.6 ± 6.0	66.2
	0.125	2.12 ± 0.04	3.25 ± 0.03	0.0379 ± 0.0007	0.0498 ± 0.0007	35.8 ± 4.8	70.2
	0.25	2.29 ± 0.07	3.04 ± 0.05	0.0415 ± 0.0005	0.0463 ± 0.0006	28.7 ± 2.6	76.2
	0.50	2.25 ± 0.05	3.06 ± 0.06	0.0370 ± 0.0006	0.0421 ± 0.0004	21.1 ± 2.0	82.5
	1.00	1.82 ± 0.01	3.21 ± 0.02	0.0420 ± 0.0003	0.0428 ± 0.0002	11.9 ± 1.4	90.1
ATA	0.0625	1.82 ± 0.04	2.77 ± 0.04	0.0456 ± 0.0001	0.0494 ± 0.0002	35.0 ± 4.5	71.0
	0.125	2.35 ± 0.08	3.06 ± 0.10	0.0391 ± 0.0004	0.0456 ± 0.0005	28.7 ± 2.4	76.2
	0.25	1.59 ± 0.10	3.25 ± 0.12	0.0407 ± 0.0005	0.0444 ± 0.0007	21.6 ± 2.5	82.1
	0.50	1.92 ± 0.03	2.71 ± 0.02	0.0389 ± 0.0006	0.0491 ± 0.0009	14.0 ± 1.3	88.4
	1.00	1.88 ± 0.05	2.90 ± 0.04	0.0400 ± 0.0004	0.0466 ± 0.0006	6.0 ± 0.3	95.0
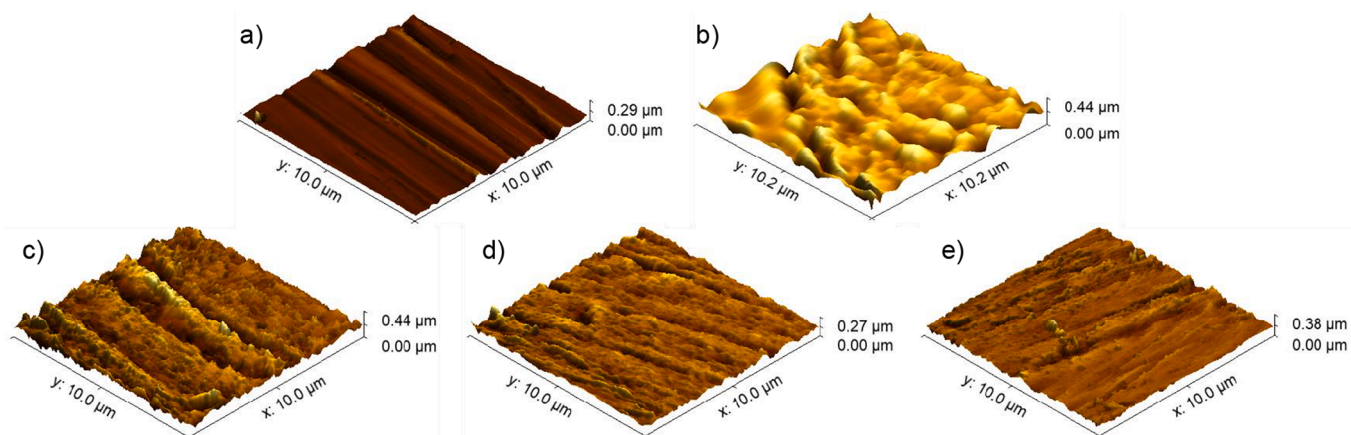
Fig. 6. AFM images for grounded (a) and corroded (b) mild steel, and in the presence of 1.00 mmol/L of TTA (c), ATM (d), and ATA (e).

without the need to previously know the Tafel constants. To measure the confidence of the experiment, causality factors 2 and 3 are used (Obot and Onyeachu, 2018). The obtained graphs are shown in Figs. S15-S17 and the data in Table 6.

From Table 6, the value of i_{corr} for the blank solution depicts a high rate of redox reactions from the corrosive process of carbon steel. As seen in other electrochemical experiments, in the lowest tested concentration (0.0625 mmol/L) all three organic compounds act as good corrosion inhibitors, lowering the corrosion current density from 120.1 to 45.4, 40.6, and 35.0 μA cm^{-2} (Machado Fernandes et al., 2022a, 2022b).

At a concentration of 1.00 mmol/L, TTA, ATM, and ATA present anticorrosive efficiency of 85.5, 90.1, and 95.0, respectively, lowering i_{corr} from 120.1 (blank solution) to 17.5, 11.9, and 6.0 μA cm^{-2}. These results confirm that all three evaluated compounds act as excellent corrosion inhibitors for 1020 mild steel in hydrochloric acid and corroborate the others obtained results (Haruna et al., 2021).

Furthermore, as previously discussed in other sections, the introduction of the three corrosion inhibitors does not modify the reaction mechanism. This observation holds true in this context as well, as evidenced by the Tafel parameters (βa and -βc), which exhibit negligible alterations in their values between uninhibited and inhibited solutions. This consistency further supports the established fact that the presence of these inhibitors does not impact the underlying reaction mechanism.

Table 7
Atomic Force Microscopy parameters.

	Average Roughness (nm)
Grounded surface	29.6
Corroded surface	141.0
1 mol/L HCl + 1.00 mmol/L TTA	68.4
1 mol/L HCl + 1.00 mmol/L ATM	56.2
1 mol/L HCl + 1.00 mmol/L ATA	50.8

3.8. Atomic force Microscopy (AFM)

It was well defined via gravimetric and electrochemical measurements that TTA, ATM, and ATA act as corrosion inhibitors via adsorption on the mild steel surface. Thus, AFM was employed to evaluate the mild steel surface topography on different moments, as shown in Fig. 6. The average roughness (R_a) of those surfaces was also calculated and is exhibited in Table 7.

From Fig. 6a, the low R_a is explained with a very smooth surface, with grounding marks from the #600 SiC-emery paper. From Fig. 6b, one can see the extreme damage caused by the aggressive medium (1 mol/L HCl) to the metallic surface, thus explaining the high roughness value. From Fig. 6c-e, much more protected and preserved surfaces are observed, with marks similar to those seen in the grounded mild steel and reasonable R_a values, suggesting the adsorption of TTA, ATM, and ATA, impeding the corrosive process (Tiwari et al., 2021).
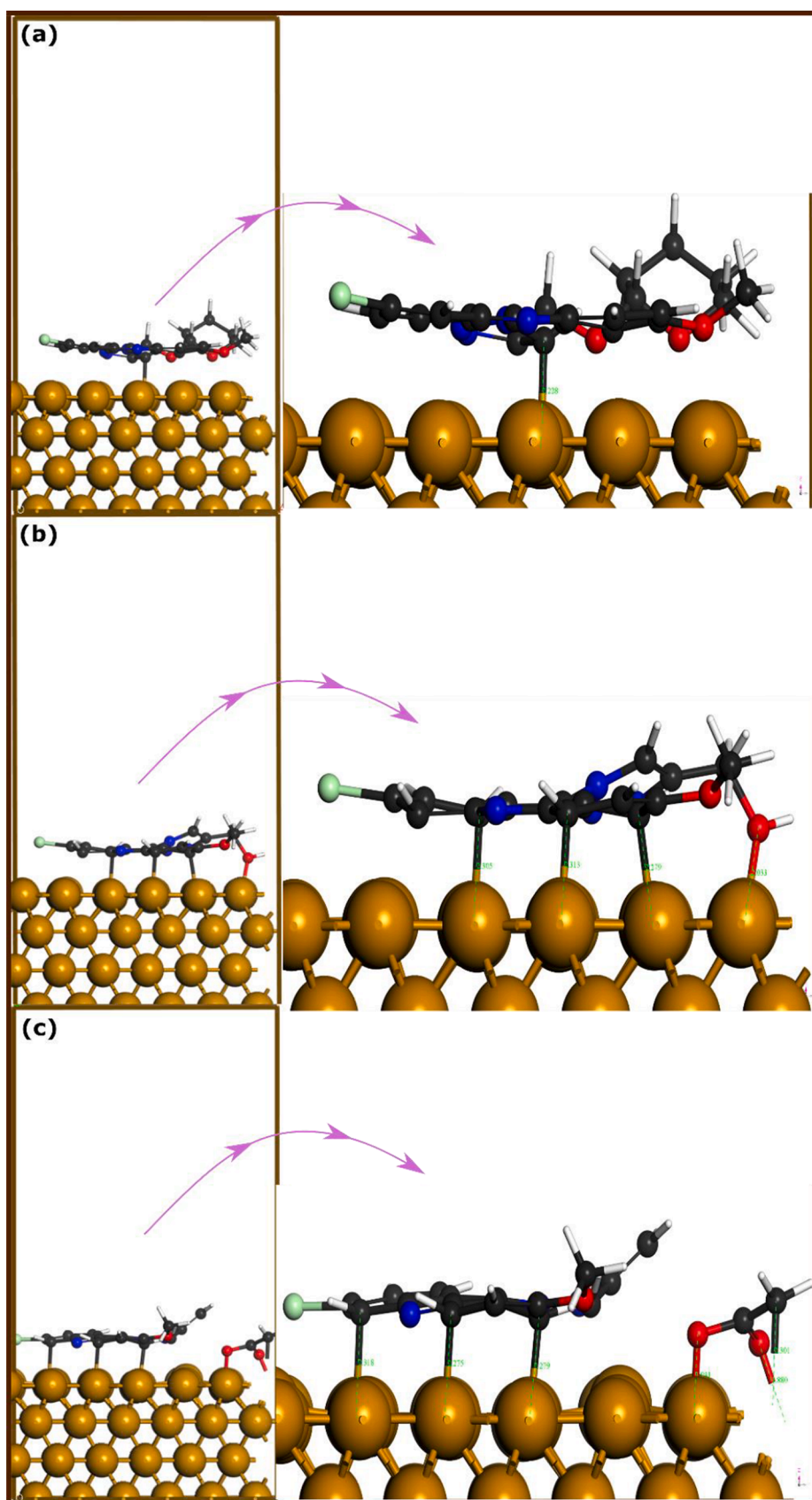
Fig. 7. DFT-optimized adsorption geometries of (a) TTA, (b) ATM, and (c) ATA molecules on Fe(1 1 0) iron surface.
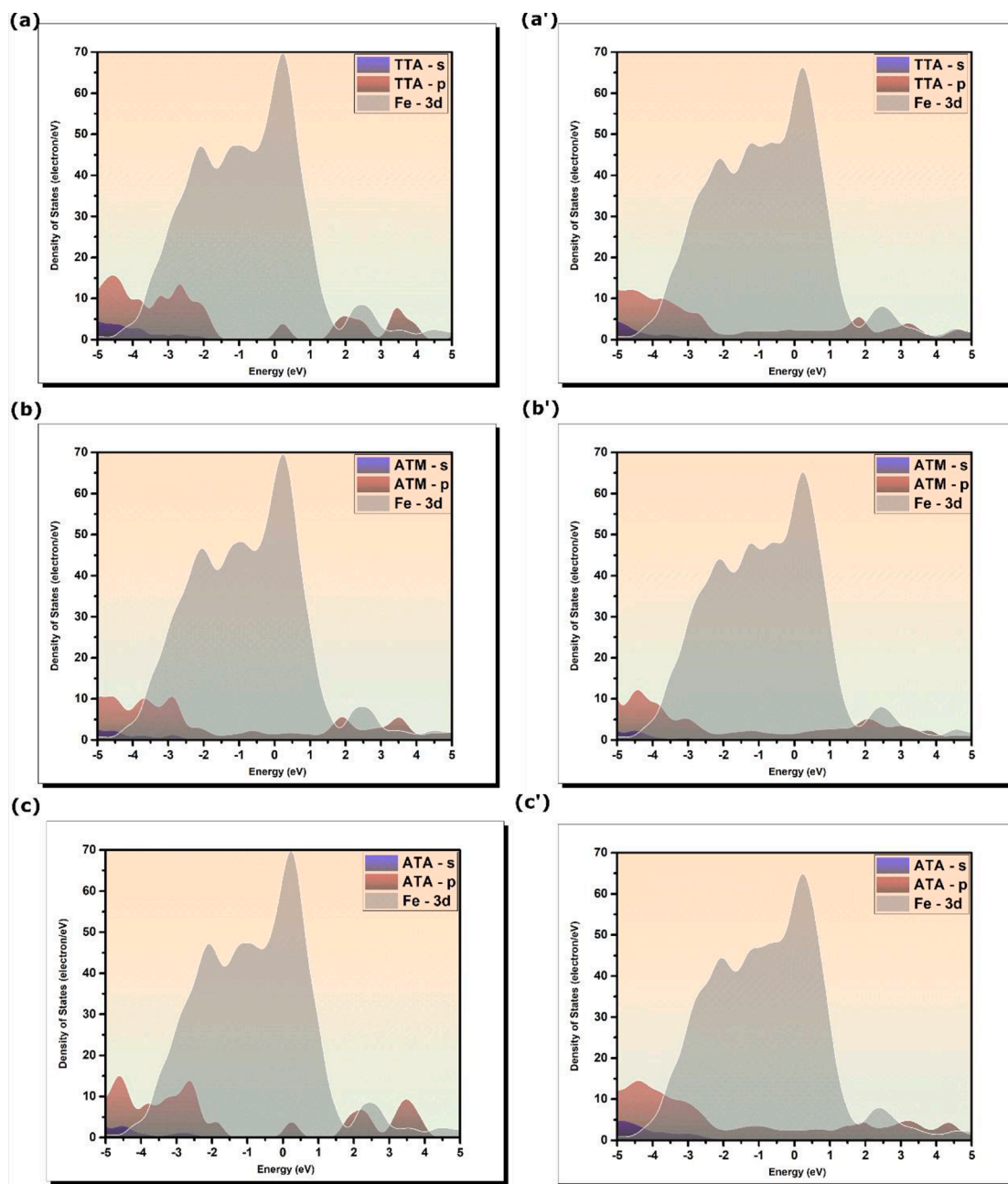
Fig. 8. Projected density of states of (a)-(b) isolated and (a')-(b') adsorbed inhibitor's molecules on Fe(1 1 0) surface.

3.9. First-principles DFT simulations

3.9.1. Geometries and energies

Investigating the inhibitor-metal interactions from experiments would be difficult to give relevant information regarding the inhibitor active sites and adsorption configurations. First-principles DFT simulation is a very promising theoretical tool to simulate inhibitor molecules' interactions with the metal surface, thus revealing insights into electronic and structural features relevant to inhibitor performance (Gustinčič and Kokalj, 2015, Kokalj, 2015, Kokalj et al., 2020).

The optimized adsorption geometries of TTA, ATM, and ATA molecules on Fe(1 1 0) surface are shown in Fig. 7. Interestingly, it can be observed that all molecules exhibit a parallel adsorption configuration on the iron surface. Although that was the initial adsorption configuration, molecules would always be in their most stable adsorption geometry. In confirmation of this interpretation, previous studies found that large-size inhibitor molecules tend to adopt a parallel disposition over metal surfaces (Guo et al., 2017, Guo et al., 2018, El-Haitout et al., 2022, El-Haitout et al., 2023). Looking now at each of the individually optimized adsorption geometry, one can notice that the TTA molecule forms only one bond with iron surface whereas ATM and ATA molecules form several bonds with iron atoms. The bond that is formed between the C atom of the TTA molecule and iron atoms has a distance length of 2.228 Å. Heteroatoms of the TTA molecule are all close to the upper layer of the iron surface, but without any bonding with iron atoms.

Moving to the ATM molecule which has a methanol attached to its triazolic nucleus, one finds that both C and O atoms bond with iron atoms while no bond involves the N atoms. The Fe-C bonds have distances of 2.279, 2.313, and 2.305 Å while Fe-O has a distance of 2.033 Å. Nitrogen atoms of ATM molecule have also a close contact with iron
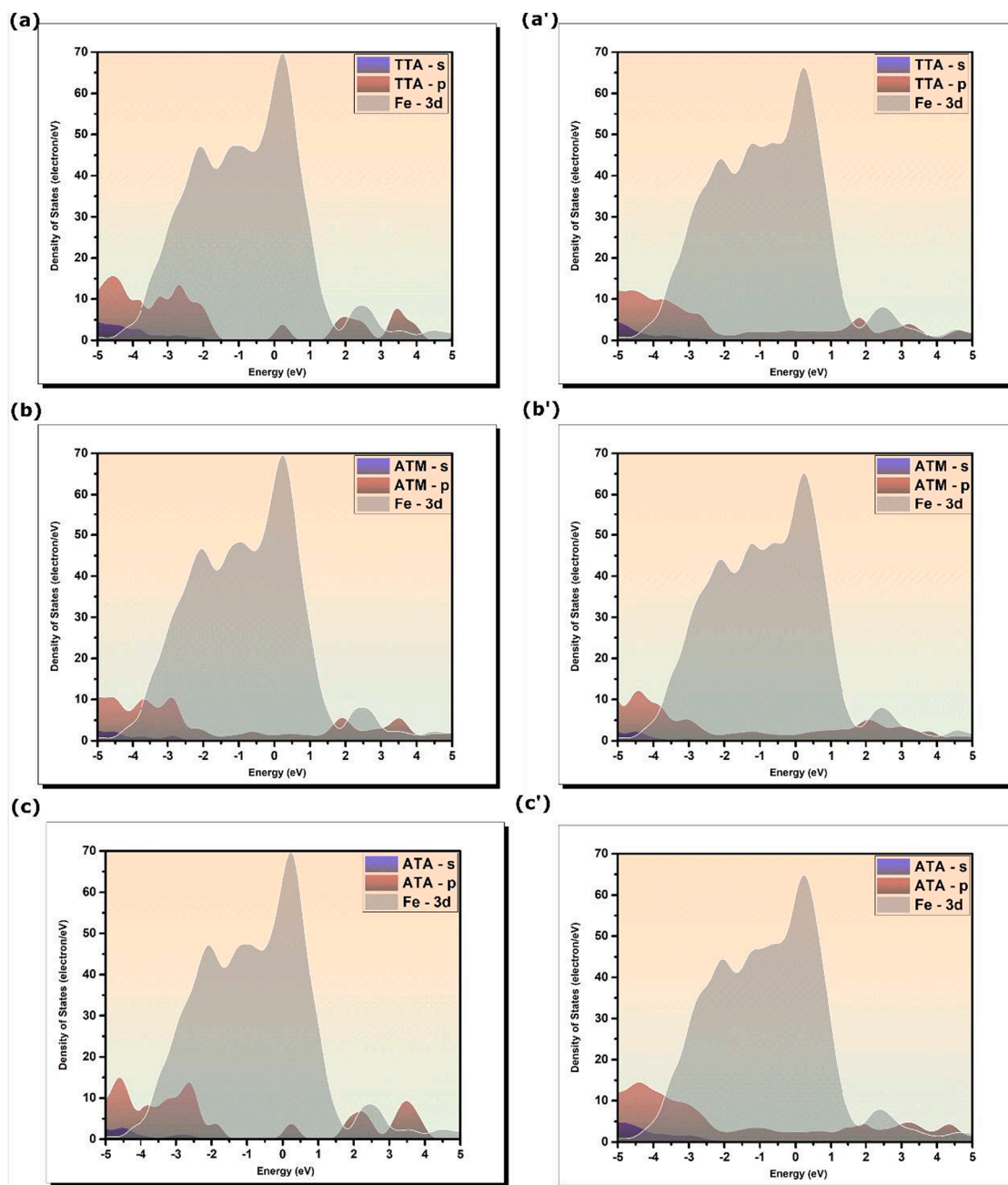
Fig. 8. (*continued*).

atoms, but no bonding is noticed. The ATA's molecule, on the other hand, ends up breaking the single bond between O and C atoms of the methyl acetate attached to the triazolic nucleus. There is formation of more bonds between ATA's atoms and iron atoms compared to the previous two molecules. The acetate moiety forms two Fe—O bonds with distance lengths of 1.88 and 1.931 Å whereas C atoms form four Fe—C bonds with distances between 2.275 and 2.318 Å.

Without looking at interaction energies of optimized adsorption systems, it seems that number of formed bonds increases in the following trend: TTA < ATM < ATA. The triazolic nucleus is substituted by 2-methoxytetrahydro-2H-pyran in the case of TTA, however, its effect on the compound's experimental inhibition performance is not significant, which is also noticeable from first-principles DFT simulations. The substitution of the triazolic nucleus by a methanol (ATM) and methyl acetate (ATA) seems to significantly change their electronic density distribution, and thus their interactive force with the iron surface,

reaching a higher corrosion inhibition performance.

Before moving to the energetic analysis of optimized adsorption geometries, it would be beneficial to compare the bond lengths of interacting molecules with their respective sum of covalent radii to get an initial idea about the nature of the formed bonds. It has been reported that the sum of the covalent radii for Fe-C ($r_C + r_{Fe}$) and Fe-O ($r_O + r_{Fe}$) are 2.08 and 1.98 Å, respectively (Cordero et al., 2008). It can then be concluded that formed bonds between TTA, ATM, and ATA's atoms and the iron surface are all covalent, a statement that can be confirmed or denied later by projected density of states analysis.

The energetic analysis reveals that TTA, ATM, and ATA have an interaction energy of -0.49, -2.53, and -2.77 eV, respectively. These values reveal no surprise results but confirm the geometrical conclusions made from optimized adsorption geometries. Once again, it can be said that substituting the triazolic nucleus with a methyl acetate or methanol is the most beneficial in terms of inhibitors' reactivity and interactions
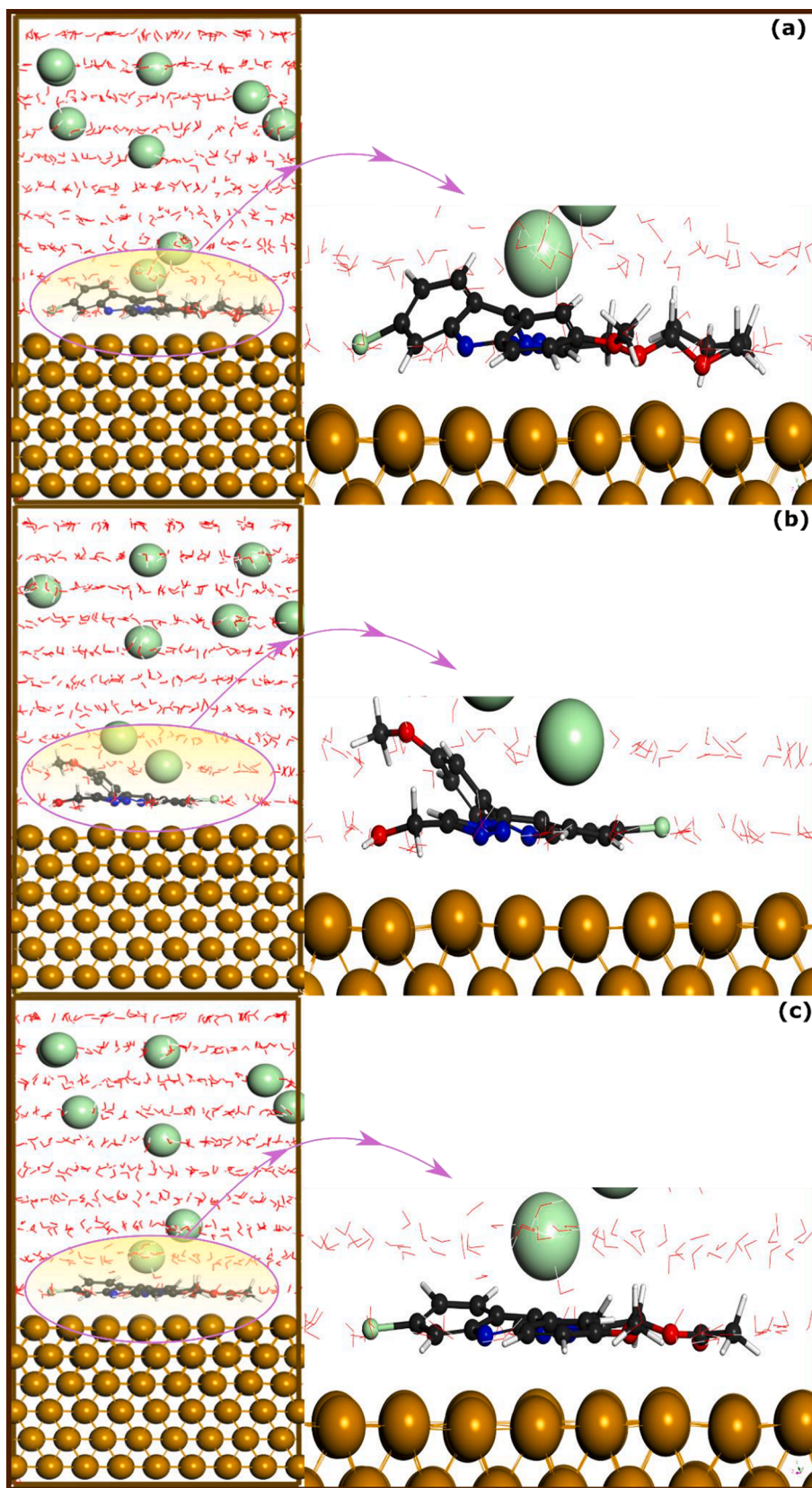
Fig. 9. The best adsorption configuration of (a) TTA, (b) ATM, and (c) ATA molecules on Fe(1 1 0) iron surface in presence of a simulated corrosive solution, obtained by molecular dynamics simulation.

with the metal surface. It highlights that the right substitution is not always related to the nature of the functional group, but other factors would influence the effectiveness of the entire compound such as the adsorption configuration and charge distribution, among others (Verma et al., 2018).

3.9.2. Projected density of states

The electronic projected density of states (PDOSs) is a useful tool to gain insights into the bonding nature of inhibitor molecules on Fe(1 1 0) surface. The plots of projected density of states of TTA, ATM, and ATA molecules in their isolated and adsorbed states are shown in Fig. 8. The substrate–adsorbate interactions can lead to considerable changes in the electronic density of states. By inspecting the PDOS plots of 3d iron orbitals and those of the isolated inhibitor molecules, one can notice that several molecules' peaks exist within the energy range of iron 3d orbital's peaks (Kumar et al., 2022). These molecular states are likely to hybridize upon adsorption of inhibitor molecules on the iron surface.

The PDOSs of adsorbed molecules show that several peaks disappear and some of them are slightly broadened and decrease in intensity. These changes are mainly a result of a strong hybridization of molecules' p-orbitals with Fe-3d orbitals (Kumar et al., 2020, Lgaz and Lee, 2022). When inhibitor molecules approach the metal surface after first step physisorption, donor–acceptor interactions will occur between molecules' active sites and iron atoms, which is nothing but a charge transfer, resulting in the formation of covalent bonds. These results confirm what has been concluded from section 3.9.1 that the formed bonds between inhibitor molecules and Fe(1 1 0) surface are covalent. Furthermore, given the fact that N atoms do not participate in any covalent bonding with iron atoms suggests that these atoms are primarily responsible for initial physical interactions with the iron surface as most of N atomic sites can easily be protonated in acidic mediums (Ebenso et al., 2021).

3.10. Molecular dynamics

Molecular dynamics simulation is one of the powerful theoretical tools that plays a growing role in various research fields. It is an attractive means for studying chemical phenomena in nanoscale; hence it is suitable for investigating the behavior of corrosion inhibitors when interacting with metal surface. Despite its known limitations in simulating bond-breaking and bond-formation along with overestimated adsorption energy (Kokalj, 2021), it is a useful way to get knowledge of adsorption configuration of molecules when interacting with metal surface in presence of a simulated solution. Herein, the best adsorption configurations of the inhibitor-Fe(1 1 0) are obtained from MD simulations as depicted in Fig. 9. From this Figure, it can be observed that all molecules tend to adopt a parallel disposition over the metal surface either completely or partially, suggesting their higher adsorption competitiveness in presence of water and corrosive particles.

ATA molecule exhibits a nearly flat disposition over the metal surface, which is not surprising given its high affinity to iron atoms as demonstrated by DFT simulation and experimental findings. The ATM molecule, on the other side, exhibits a partially flat disposition over the iron surface through its triazolic nucleus and chlorophenyl part, which seems to be in line with DFTB results. Concerning the TTA molecule, it can be seen that it also exhibits a partial parallel adsorption on the metal surface through its triazolic nucleus, and the substituted group attached to it. These results highlight that, in the presence of a solution, the three molecules have a high ability to adsorb on the metal surface. This adsorption, which occurs in a nearly flat adsorption mode, can maximize the interaction of molecules' reactive sites with iron atoms, forming a protective layer that prevents acid corrosion (Saha et al., 2018).

4. Conclusions

Three new 1,2,3-triazolyl-acridine derivatives were synthetized in good yields via a simple two steps synthetic procedure involving a fast ultrasound CuAAC strategy and evaluated as corrosion inhibitor for mild steel in acidic media. Gravimetric experiments showed anticorrosive efficiencies of 85, 90, and 94 % for TTA, ATM, and ATA, respectively, at 1 mmol/L and room temperature. All three organic molecules displayed even better results at both 318 and 338 K, proving to be excellent corrosion inhibitors. The tested compounds followed the Langmuir adsorption theory of monolayer formation. EIS showed an increased charge transfer resistance in the presence of TTA, ATM, and ATA, with lower double layer capacitance values. Polarization curves confirmed that they all are mixed-type corrosion inhibitors and EFM proved that the presence of the organic compounds in the acidic media resulted in lower corrosion density currents, protecting the mild steel from redox reactions arising from the corrosive process. AFM images exhibited the topography of the 1020 mild steel surface and indicated the presence of a protective film. First-principles DFT simulation indicated that molecules of the three investigated compounds can covalently bond with iron atoms with ATA molecule showed a bon-breaking behavior upon interaction with iron atoms. As demonstrated from projected density of states analysis, the bonds formed between inhibitors' molecules and iron atoms were due to strong charge transfer. Molecular dynamics simulation revealed that the three molecules can exhibit a nearly flat disposition over the iron surface in presence of water and corrosive particles. Experimental and theoretical simulations gave strong evidence about the ability of the novel developed compounds to prevent acid corrosion when added to HCl solution.

Declaration of Competing Interest

The authors declare that they have no known competing financial interests or personal relationships that could have appeared to influence the work reported in this paper.

Appendix A. Supplementary material

Supplementary data to this article can be found online at https://doi.org/10.1016/j.arabjc.2023.105401.

References

Akpan, E.D., Isaac, I.O., Olasunkanmi, L.O., et al., 2019. Acridine-based thiosemicarbazones as novel inhibitors of mild steel corrosion in 1 M HCl: synthesis, electrochemical, DFT and Monte Carlo simulation studies. RSC Adv. 9, 29590–29599. https://doi.org/10.1039/C9RA04778F.

Akpan, E.D., Dagdag, O., Ebenso, E.E., 2022. Recent progress on the anticorrosion activities of acridine and acridone derivatives: a review. J. Mol. Liq. 361, 119686.

Al Jahdaly, B.A., 2023. Rosmarinus officinalis extract as eco-friendly corrosion inhibitor for copper in 1 M nitric acid solution: experimental and theoretical studies. Arab. J. Chem. 16 https://doi.org/10.1016/j.arabjc.2022.104411.

AlSalhi, M.S., Devanesan, S., Rajasekar, A., et al., 2023. Characterization of plants and seaweeds based corrosion inhibitors against microbially influenced corrosion in a cooling tower water environment. Arab. J. Chem. 16 https://doi.org/10.1016/j.arabjc.2022.104513.

Altunbaş Şahin, E., 2022. Experimental and theoretical studies of acridine orange as corrosion inhibitor for copper protection in acidic media. J. Indian Chem. Soc. 99, 100358.

Andrés Coy-Barrera, C., Camilo Monge, I., Quiroga, D., 2023. Non-soluble chalcones and their potential application as corrosion coatings on carbon steel exposed to 1 M HCl solutions. Arab. J. Chem. 16 https://doi.org/10.1016/j.arabjc.2022.104459.

Bashir, S., Thakur, A., Lgaz, H., et al., 2020. Corrosion inhibition efficiency of bronopol on aluminium in 0.5 M HCl solution: insights from experimental and quantum chemical studies. Surf. Interfaces 20. https://doi.org/10.1016/j.surfin.2020.100542.

Boutouil, A., Laamari, M.R., Elazhary, I., et al., 2020. Towards a deeper understanding of the inhibition mechanism of a new 1,2,3-triazole derivative for mild steel corrosion in the hydrochloric acid solution using coupled experimental and theoretical methods. Mater. Chem. Phys. 241, 122420.

Brug, G.J., van den Eeden, A.L.G., Sluyters-Rehbach, M., et al., 1984. The analysis of electrode impedances complicated by the presence of a constant phase element. J. Electroanal. Chem. Interfacial Electrochem. 176, 275–295. https://doi.org/10.1016/S0022-0728(84)80324-1.

Chaouiki, A., Chafiq, M., Al-Moubaraki, A.H., et al., 2022. Electrochemical behavior and interfacial bonding mechanism of new synthesized carbocyclic inhibitor for exceptional corrosion resistance of steel alloy: DFTB, MD and experimental approaches. Arab. J. Chem. 15 https://doi.org/10.1016/j.arabjc.2022.104323.

Cherrad, S., Alrashdi, A.A., Lee, H.-S., et al., 2022. *Cupressus arizonica* fruit essential oil: a novel green inhibitor for acid corrosion of carbon steel. Arab. J. Chem. 15 https://doi.org/10.1016/j.arabjc.2022.103849.

Clark, S.J., Segall, M.D., Pickard, C.J., et al., 2005. First principles methods using CASTEP. Zeitschrift Für Kristallographie - Crystalline Mater. 220, 567–570.

Cordero, B., Gómez, V., Platero-Prats, A.E., et al., 2008. Covalent radii revisited. Dalton Trans. 2832–2838 https://doi.org/10.1039/B801115J.

Damej, M., Kaya, S., El Ibrahimi, B., et al., 2021. The corrosion inhibition and adsorption behavior of mercaptobenzimidazole and bis-mercaptobenzimidazole on carbon steel in 1.0 M HCl: experimental and computational insights. Surf. Interfaces 24. https://doi.org/10.1016/j.surfin.2021.101095.

de Sampaio, M.T.G., Fernandes, C.M., de Souza, G.G.P., et al., 2020. Evaluation of aqueous extract of *Mandevilla fragrans* leaves as environmental-friendly corrosion inhibitor for mild steel in acid medium. J. Bio- and Tribo-Corrosion 7. https://doi.org/10.1007/s40735-020-00445-9.

Ebenso, E.E., Verma, C., Olasunkanmi, L.O., et al., 2021. Molecular modelling of compounds used for corrosion inhibition studies: a review. PCCP 23, 19987–20027. https://doi.org/10.1039/D1CP00244A.

El Faydy, M., Benhiba, F., Warad, I., et al., 2022. Experimental and theoretical investigations of two quinolin-8-ol derivatives as inhibitors for carbon steel in 1 M HCl solution. J. Phys. Chem. Solid 165, 110699. https://doi.org/10.1016/j.jpcs.2022.110699.

Elazhary, I., Laamari, M.R., Boutouil, A., et al., 2019. Comparative study of 1,2,3-triazole derivatives as corrosion inhibitors of mild steel in sulphuric acid solution. Anti-Corros. Methods Mater. 66, 544–555. https://doi.org/10.1108/acmm-10-2018-2018.

El-Haitout, B., Hejjaj, C., Lgaz, H., et al., 2022. Superior long-term corrosion inhibition of N80 steel by new eco-friendly hydrazone-based compounds in a simulated oil well acidizing environment: establishing the mechanism at the molecular level. Langmuir 38, 15937–15949. https://doi.org/10.1021/acs.langmuir.2c02132.

El-Haitout, B., Selatnia, I., Lgaz, H., et al., 2023. Exploring the feasibility of new eco-friendly heterocyclic compounds for establishing efficient corrosion protection for N80 steel in a simulated oil well acidizing environment: from molecular-level prediction to experimental validation. Colloids Surf. A Physicochem. Eng. Asp 656, 130372. https://doi.org/10.1016/j.colsurfa.2022.130372.

El-Lateef, H.M.A., Shaaban, S., Shalabi, K., et al., 2022. Novel organoselenium-based N-mealanilic acids as efficacious corrosion inhibitors for 6061 aluminum alloy in molar HCl: in-silico modeling, electrochemical, and surface morphology studies. J. Taiwan Inst. Chem. Eng. 133 https://doi.org/10.1016/j.jtice.2022.104258.

En-Nylly, M., Skal, S., El Aoufir, Y., et al., 2023. Performance evaluation and assessment of the corrosion inhibition mechanism of carbon steel in HCl medium by a new hydrazone compound: Insights from experimental, DFT and first-principles DFT simulations. Arabian J. Chem. 16 https://doi.org/10.1016/j.arabjc.2023.104711.

Espinoza Vázquez, A., González-Olvera, R., Moreno Cerros, D., et al., 2021. Inhibition of acid corrosion in API 5L X52 steel with 1,2,3-triazole derivatized from benzyl alcohol: experimental and theoretical studies. J. Mol. Struct. 1242, 130731 https://doi.org/10.1016/j.molstruc.2021.130731.

Espinoza-Vázquez, A., Negrón-Silva, G.E., González-Olvera, R., et al., 2016. Effect of hydrodynamic conditions, temperature and immersion times on the corrosion inhibition efficiency of API 5L X52 Steel in 1M HCl containing 1H–1,2,4 or 1H–1,2,3-triazoles. Arab. J. Sci. Eng. 42, 163–174. https://doi.org/10.1007/s13369-016-2116-4.

Faydy, M.E., Rbaa, M., Lakhrissi, L., et al., 2019. Corrosion protection of carbon steel by two newly synthesized benzimidazol-2-ones substituted 8-hydroxyquinoline derivatives in 1 M HCl: experimental and theoretical study. Surf. Interfaces 14, 222–237. https://doi.org/10.1016/j.surfin.2019.01.005.

Fernandes, C.M., Alvarez, L.X., dos Santos, N.E., et al., 2019a. Green synthesis of 1-benzyl-4-phenyl-1H-1,2,3-triazole, its application as corrosion inhibitor for mild steel in acidic medium and new approach of classical electrochemical analyses. Corros. Sci. 149, 185–194. https://doi.org/10.1016/j.corsci.2019.01.019.

Fernandes, C.M., Ferreira Fagundes, T.D.S., Escarpini dos Santos, N., et al., 2019b. Ircinia strobilina crude extract as corrosion inhibitor for mild steel in acid medium. Electrochimica Acta. 312, 137–148. https://doi.org/10.1016/j.electacta.2019.04.148.

Fernandes, C.M., Mello, M.V.P., dos Santos, N.E., et al., 2019c. Theoretical and experimental studies of a new aniline derivative corrosion inhibitor for mild steel in acid medium. Mater. Corros. 71, 280–291. https://doi.org/10.1002/maco.201911065.

Fernandes, C.M., Fagundes, T.D.S.F., dos Santos, N.E., et al., 2020. Marine octocoral phyllogorgia dilatata: identification of sesquiterpenes and activity as a natural and renewable corrosion inhibitor. Analytical Bioanalytical Electrochem. 12, 437–457.

Fernandes, C.M., de Oliveira, P.C.O., Pina, V.G.S.S., et al., 2022a. Pyrolysis of Syagrus coronata: transforming agroindustrial waste into a new environmentally sustainable corrosion inhibitor. Sustain. Chem. Pharm. 29 https://doi.org/10.1016/j.scp.2022.100751.

Fernandes, C.M., Pina, V.G.S.S., Alfaro, C.G., et al., 2022b. Innovative characterization of original green vanillin-derived schiff bases as corrosion inhibitors by a synergic approach based on electrochemistry, microstructure, and computational analyses. Colloids Surf A Physicochem Eng Asp 128540. https://doi.org/10.1016/j.colsurfa.2022.128540.

Guo, L., Qi, C., Zheng, X., et al., 2017. Toward understanding the adsorption mechanism of large size organic corrosion inhibitors on an Fe(110) surface using the DFTB method. RSC Adv. 7, 29042–29050. https://doi.org/10.1039/C7RA04120A.

Guo, L., Wu, M., Kaya, S., et al., 2018. Influence of the alkyl chain length of alkyltriazoles on the corrosion inhibition of iron: a DFTB study. AIP Conf. Proc. 1995, 020015 https://doi.org/10.1063/1.5048746.

Gustinčič, D., Kokalj, A., 2015. A DFT study of adsorption of imidazole, triazole, and tetrazole on oxidized copper surfaces: Cu2O(111) and Cu2O(111)-w/o-CuCUS. PCCP 17, 28602–28615. https://doi.org/10.1039/C5CP03647J.

Hajjaji, F.E., Salim, R., Taleb, M., et al., 2021. Pyridinium-based ionic liquids as novel eco-friendly corrosion inhibitors for mild steel in molar hydrochloric acid: experimental & computational approach. Surf. Interfaces 22. https://doi.org/10.1016/j.surfin.2020.100881.

Haruna, K., Alhems, L.M., Saleh, T.A., 2021. Graphene oxide grafted with dopamine as an efficient corrosion inhibitor for oil well acidizing environments. Surf. Interfaces 24. https://doi.org/10.1016/j.surfin.2021.101046.

Hrimla, M., Bahsis, L., Boutouil, A., et al., 2021. Corrosion inhibition performance of a structurally well-defined 1,2,3-triazole derivative on mild steel-hydrochloric acid interface. J. Mol. Struct. 1231 https://doi.org/10.1016/j.molstruc.2021.129895.

Hrimla, M., Bahsis, L., Laamari, M.R., et al., 2022. An overview on the performance of triazole derivatives as corrosion inhibitors for metal surfaces. Journal 23. https://doi.org/10.3390/ijms23010016.

Jiang, H., Wang, B., Liu, J., et al., 2023. Corrosion inhibition of Q235 and X65 steels in CO2-saturated solution by 2-phenyl imidazoline. Arab. J. Chem. 16 https://doi.org/10.1016/j.arabjc.2023.104774.

Kaskah, S.E., Pfeiffer, M., Klock, H., et al., 2017. Surface protection of low carbon steel with N-acyl sarcosine derivatives as green corrosion inhibitors. Surf. Interfaces 9, 70–78. https://doi.org/10.1016/j.surfin.2017.08.002.

Kokalj, A., 2015. Ab initio modeling of the bonding of benzotriazole corrosion inhibitor to reduced and oxidized copper surfaces. Faraday Discuss. 180, 415–438. https://doi.org/10.1039/C4FD00257A.

Kokalj, A., 2021. Molecular modeling of organic corrosion inhibitors: calculations, pitfalls, and conceptualization of molecule–surface bonding. Corros. Sci. 193, 109650 https://doi.org/10.1016/j.corsci.2021.109650.

Kokalj, A., Behzadi, H., Farahati, R., 2020. DFT study of aqueous-phase adsorption of cysteine and penicillamine on Fe(110): Role of bond-breaking upon adsorption. Appl. Surf. Sci. 514, 145896 https://doi.org/10.1016/j.apsusc.2020.145896.

Kumar, D., Jain, V., Rai, B., 2020. Imidazole derivatives as corrosion inhibitors for copper: a DFT and reactive force field study. Corros. Sci. 171, 108724 https://doi.org/10.1016/j.corsci.2020.108724.

Kumar, D., Jain, V., Rai, B., 2022. Capturing the synergistic effects between corrosion inhibitor molecules using density functional theory and ReaxFF simulations - A case for benzyl azide and butyn-1-ol on Cu surface. Corros. Sci. 195, 109960 https://doi.org/10.1016/j.corsci.2021.109960.

Lgaz, H., Lee, H.-S., 2022. Facile preparation of new hydrazone compounds and their application for long-term corrosion inhibition of N80 steel in 15% HCl: an experimental study combined with DFTB calculations. J. Mol. Liq. 347, 117952 https://doi.org/10.1016/j.molliq.2021.117952.

Liu, X., Gao, Y., Gao, Y., et al., 2023. Synthesis of polyaspartic acid-glycidyl adduct and evaluation of its scale inhibition performance and corrosion inhibition capacity for Q235 steel applications. Arab. J. Chem. 16 https://doi.org/10.1016/j.arabjc.2022.104515.

Ma, Q., Qi, S., He, X., et al., 2017. 1,2,3-Triazole derivatives as corrosion inhibitors for mild steel in acidic medium: Experimental and computational chemistry studies. Corros. Sci. 129, 91–101. https://doi.org/10.1016/j.corsci.2017.09.025.

Machado Fernandes, C., Faro, L.V., Pina, V.G.S.S., et al., 2020a. Study of three new halogenated oxoquinolinecarbohydrazide N-phosphonate derivatives as corrosion inhibitor for mild steel in acid environment. Surf. Interfaces 21. https://doi.org/10.1016/j.surfin.2020.100773.

Machado Fernandes, C., Pina, V.G.S.S., Alvarez, L.X., et al., 2020b. Use of a theoretical prediction method and quantum chemical calculations for the design, synthesis and experimental evaluation of three green corrosion inhibitors for mild steel. Colloids Surf A Physicochem Eng Asp 599. https://doi.org/10.1016/j.colsurfa.2020.124857.

Machado Fernandes, C., Guedes, L., Alvarez, L.X., et al., 2022a. Anticorrosive properties of green-synthetized benzylidene derivatives for mild steel in hydrochloric acid: An experimental study combined with DFTB and molecular dynamics simulations. J. Mol. Liq. 363 https://doi.org/10.1016/j.molliq.2022.119790.

Machado Fernandes, C., Palmeira-Mello, M.V., Leite, M.C., et al., 2022b. Corrosion inhibition and ecotoxicological assessment of 1,2,3-triazolic alcohols. Mater. Chem. Phys. 290 https://doi.org/10.1016/j.matchemphys.2022.126508.

Machado Fernandes, C., Costa, A.R.P., Leite, M.C., et al., 2023. A detailed experimental performance of 4-quinolone derivatives as corrosion inhibitors for mild steel in acid media combined with first-principles DFT simulations of bond breaking upon adsorption. J. Mol. Liq. 375, 121299 https://doi.org/10.1016/j.molliq.2023.121299.

Martyna, G.J., Klein, M.L., Tuckerman, M., 1992. Nosé-Hoover chains: the canonical ensemble via continuous dynamics. J. Chem. Phys. 97, 2635–2643. https://doi.org/10.1063/1.463940.

Molaeipour, P., Ramezanzadeh, M., Ramezanzadeh, B., 2022. Stachys byzantina extract: A green biocompatible molecules source for graphene skeletons generation on the carbon steel for superior corrosion mitigation. Bioelectrochemistry 143, 107970. https://doi.org/10.1016/j.bioelechem.2021.107970.

Mourya, P., Banerjee, S., Singh, M.M., 2014. Corrosion inhibition of mild steel in acidic solution by Tagetes erecta (Marigold flower) extract as a green inhibitor. Corros. Sci. 85, 352–363. https://doi.org/10.1016/j.corsci.2014.04.036.

Nahlé, A., Salim, R., El Hajjaji, F., et al., 2022. Experimental and theoretical approach for novel imidazolium ionic liquids as Smart Corrosion inhibitors for mild steel in 1.0 M hydrochloric acid. Arab. J. Chem. 15 https://doi.org/10.1016/j.arabjc.2022.103967.

Noor, E.A., Al-Moubaraki, A.H., 2008. Thermodynamic study of metal corrosion and inhibitor adsorption processes in mild steel/1-methyl-4[4′-(-X)-styryl pyridinium iodides/hydrochloric acid systems. Mater. Chem. Phys. 110, 145–154. https://doi.org/10.1016/j.matchemphys.2008.01.028.

Obot, I.B., Haruna, K., Saleh, T.A., 2018. Atomistic simulation: a unique and powerful computational tool for corrosion inhibition research. Arab. J. Sci. Eng. 44, 1–32. https://doi.org/10.1007/s13369-018-3605-4.

Obot, I.B., Onyeachu, I.B., 2018. Electrochemical frequency modulation (EFM) technique: Theory and recent practical applications in corrosion research. J. Mol. Liq. 249, 83–96. https://doi.org/10.1016/j.molliq.2017.11.006.

Olasunkanmi, L.O., Idris, A.O., Adewole, A.H., et al., 2020. Adsorption and corrosion inhibition potentials of salicylaldehyde-based Schiff Bases of semicarbazide and p-toluidine on mild steel in acidic medium: experimental and computational studies. Surf. Interfaces 21. https://doi.org/10.1016/j.surfin.2020.100782.

Parlak, A.E., Omar, R.A., Koparir, P., et al., 2022. Experimental, DFT and theoretical corrosion study for 4-(((4-ethyl-5-(thiophen-2-yl)-4H-1,2,4-triazole-3-yl)thio)methyl)-7,8-dimethyl-2H-chromen-2-one. Arab. J. Chem. 15 https://doi.org/10.1016/j.arabjc.2022.104088.

Perdew, J.P., Burke, K., Ernzerhof, M., 1996. Generalized gradient approximation made simple. Phys. Rev. Lett. 77, 3865–3868. https://doi.org/10.1103/PhysRevLett.77.3865.

Popova, A., Sokolova, E., Raicheva, S., et al., 2003. AC and DC study of the temperature effect on mild steel corrosion in acid media in the presence of benzimidazole derivatives. Corros. Sci. 45, 33–58. https://doi.org/10.1016/S0010-938X(02)00072-0.

Rajamohan, N., Said Zahir Said Al Shibli, F., Rajasimman, M., 2022a. Environmentally benign Prosopis juliflora extract for corrosion protection by sorption - Gravimetric, mechanistic and thermodynamic studies. Environ Res. 203, 111816 https://doi.org/10.1016/j.envres.2021.111816.

Rajamohan, N., Zahir Said Al Shibli, F.S., Rajasimman, M., et al., 2022b. Eco-friendly biomass from Ziziphus spina-christi for protection of carbon steel in acidic conditions - Parameter effects and corrosion mechanism studies. Chemosphere. 291, 132756 https://doi.org/10.1016/j.chemosphere.2021.132756.

Rbaa, M., Abousalem, A.S., Rouifi, Z., et al., 2020. Synthesis, antibacterial study and corrosion inhibition potential of newly synthesis oxathiolan and triazole derivatives of 8-hydroxyquinoline: experimental and theoretical approach. Surf. Interfaces 19. https://doi.org/10.1016/j.surfin.2020.100468.

Rbaa, M., Lakhrissi, B., 2019. Novel oxazole and imidazole based on 8-hydroxyquinoline as a corrosion inhibition of mild steel in HCl solution: insights from experimental and computational studies. Surf. Interfaces 15, 43–59. https://doi.org/10.1016/j.surfin.2019.01.010.

Ren, S., Cui, M., Chen, X., et al., 2022. Comparative study on corrosion inhibition of N doped and N, S codoped Carbon Dots for carbon steel in strong acidic solution. J. Colloid Interface Sci. https://doi.org/10.1016/j.jcis.2022.08.070.

Saha, S.K., Murmu, M., Murmu, N.C., et al., 2018. Molecular level insights for the corrosion inhibition effectiveness of three amine derivatives on the carbon steel surface in the adverse medium: a combined density functional theory and molecular dynamics simulation study. Surf. Interfaces 10, 65–73. https://doi.org/10.1016/j.surfin.2017.11.007.

Silva, B.N.M., Pinto, A.C., Silva, F.C., et al., 2016. Ultrasound-Assisted Synthesis of Isatin-Type 5'-(4-Alkyl/Aryl-1<i>H</i>-1,2,3-triazoles) via 1,3-Dipolar Cycloaddition Reactions. J. Braz. Chem. Soc. 27.

Sun, H., 1998. COMPASS: an ab initio force-field optimized for condensed-phase applications overview with details on alkane and benzene compounds. J. Phys. Chem. B 102, 7338–7364. https://doi.org/10.1021/jp980939v.

Swope, W.C., Andersen, H.C., Berens, P.H., et al., 1982. A computer simulation method for the calculation of equilibrium constants for the formation of physical clusters of molecules: application to small water clusters. J. Chem. Phys. 76, 637–649. https://doi.org/10.1063/1.442716.

Tan, B., Zhang, S., Cao, X., et al., 2022. Insight into the anti-corrosion performance of two food flavors as eco-friendly and ultra-high performance inhibitors for copper in sulfuric acid medium. J Colloid Interface Sci. 609, 838–851. https://doi.org/10.1016/j.jcis.2021.11.085.

Tiwari, N., Mitra, R.K., Yadav, M., 2021. Corrosion protection of petroleum oil well/tubing steel using thiadiazolines as efficient corrosion inhibitor: experimental and theoretical investigation. Surf. Interfaces 22. https://doi.org/10.1016/j.surfin.2020.100770.

Verma, C., Olasunkanmi, L.O., Ebenso, E.E., et al., 2018. Substituents effect on corrosion inhibition performance of organic compounds in aggressive ionic solutions: a review. J. Mol. Liq. 251, 100–118.

Wu, Q., Jia, X., Wong, M., 2022. Effects of number, type and length of the alkyl-chain on the structure and property of indazole derivatives used as corrosion inhibitors. Mater. Today Chem. 23 https://doi.org/10.1016/j.mtchem.2021.100636.

Zaher, A., Aslam, R., Lee, H.-S., et al., 2022. A combined computational & electrochemical exploration of the Ammi visnaga L. extract as a green corrosion inhibitor for carbon steel in HCl solution. Arab. J. Chem. 15 https://doi.org/10.1016/j.arabjc.2021.103573.

Zhang, W., Li, H.-J., Wang, M., et al., 2018. Halogen-substituted acridines as highly effective corrosion inhibitors for mild steel in acid medium. J. Phys. Chem. C 122, 25349–25364. https://doi.org/10.1021/acs.jpcc.8b07015.

Zhang, W., Li, H.-J., Wang, M., et al., 2019a. Tetrahydroacridines as corrosion inhibitor for X80 steel corrosion in simulated acidic oilfield water. J. Mol. Liq. 293, 111478.

Zhang, W., Chen, L., Wu, Y.-C., et al., 2020a. Preparation of methylacridinium iodides self-assembled monolayers and its anti-corrosion properties for mild steel in seawater: experimental and computational studies. J. Mol. Liq. 313, 113545.

Zhang, W., Li, H.-J., Chen, L., et al., 2020b. Performance and mechanism of a composite scaling–corrosion inhibitor used in seawater: 10-Methylacridinium iodide and sodium citrate. Desalination 486, 114482.

Zhang, Q.H., Li, Y.Y., Lei, Y., et al., 2022. Comparison of the synergistic inhibition mechanism of two eco-friendly amino acids combined corrosion inhibitors for carbon steel pipelines in oil and gas production. Appl. Surf. Sci. 583 https://doi.org/10.1016/j.apsusc.2022.152559.

Zhang, W., Wang, Y., Li, H.-J., et al., 2019b. Synergistic Inhibition Effect of 9-(4-Chlorophenyl)-1,2,3,4-tetrahydroacridines and Tween-80 for mild steel corrosion in acid medium. J. Phys. Chem. C 123, 14480–14489. https://doi.org/10.1021/acs.jpcc.9b02595.

Zhang, W., Liu, Y., Zhang, Y., et al., 2020c. 9-Substituted acridines as effective corrosion inhibitors for mild steel: electrochemical, surface morphology, and computational studies. New J. Chem. 44, 6464–6474. https://doi.org/10.1039/D0NJ00440E.

Zheng, Z., Hu, J., Eliaz, N., et al., 2022. Mercaptopropionic acid-modified oleic imidazoline as a highly efficient corrosion inhibitor for carbon steel in CO₂-saturated formation water. Corros. Sci. 194 https://doi.org/10.1016/j.corsci.2021.109930.

Zulkifli, F., Ali, N.A., Yusof, M.S.M., et al., 2017. Henna leaves extract as a corrosion inhibitor in acrylic resin coating. Prog. Organic Coatings 105, 310–319. https://doi.org/10.1016/j.porgcoat.2017.01.017.